UCSF

Title

Identifying emergent regulatory behaviors of the PINK1/Parkin mitophagy decision circuit

Permalink

https://escholarship.org/uc/item/9p94b7x7

Author

waters, christopher stone

Publication Date

2023

Peer reviewed|Thesis/dissertation

Identifying emergent regulatory behaviors of the PINK1/Parkin mitophagy decision circuit
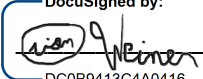
by
Christopher Waters

DISSERTATION
Submitted in partial satisfaction of the requirements for degree of
DOCTOR OF PHILOSOPHY

in

Cell Biology

in the

GRADUATE DIVISION
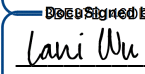of the
UNIVERSITY OF CALIFORNIA, SAN FRANCISCO

Approved:

DocuSigned by:
_____   Orion Weiner
DC0B9413C4A0416...   Chair

DocuSigned by:
_____   Jayanta Debnath
_____24F0...

DocuSigned by:
Steven Altschuler   Steven Altschuler
_____9437...

DocuSigned by:
Lani Wu   Lani Wu
6F84CA582ABA4BF...

_____
                                              Committee Members

CONTRIBUTIONS

Chapter 1: Adapted from the published manuscript: **Waters, C.S.**, Angenent, S.W., Altschuler, S.J., Wu, L.F. (2023). A PINK1 input threshold arises from positive feedback in the PINK1/Parkin mitophagy decision circuit. Cell Reports. doi: 10.1016/j.celrep.2023.113260

Identifying emergent regulatory behaviors of the PINK1/Parkin mitophagy decision circuit

Christopher Waters

ABSTRACT

Mitochondria accumulate damage over time. Cells maintain a healthy pool of mitochondria by targeting damaged mitochondria for mitophagy (mitochondrial degradation) via the PINK1/Parkin biological circuit. Specifically, the kinase PINK1 accumulates on the surface of damaged mitochondria, where it triggers activation of a positive feedback loop involving Parkin. Activation of this positive feedback loop targets damaged mitochondria for lysosomal degradation (mitophagy). However, PINK1 is also present, at low levels, on healthy mitochondria where it could errantly activate the positive feedback loop and target healthy mitochondria for degradation. How, then, does the PINK1/Parkin circuit interpret mitochondrial PINK1 concentrations to differentiate between healthy and damaged mitochondria?

Here, I applied principles of systems and cell biology to identify emergent behaviors that could allow the PINK1/Parkin circuit to distinguish between damaged and healthy mitochondria. Using a synthetic circuit approach, I mapped the circuit's activation response (Parkin recruitment to mitochondria) across a range of circuit input levels (PINK1 concentration on mitochondria). I found that Parkin is only recruited to mitochondria when the mitochondrial PINK1 concentration exceeds a threshold, and then only after a delay that is inversely proportional to PINK1 concentration. Next, I used a combination of PINK1 and Parkin mutants, to explore the dependencies of the identified regulatory behaviors. I found that both the PINK1 input threshold and the input-reciprocal activation delay behaviors are linked to the circuit's positive feedback architecture, termed here as input-coupled positive feedback. Finally, I collaborated with a

mathematician to show that input-coupled positive feedback in the PINK1/Parkin circuit is sufficient to generate these two regulatory behaviors. In sum, these results describe a pair of emergent regulatory properties that can allow the PINK1/Parkin positive feedback circuit to avoid activation on healthy mitochondria by interpreting the strength and duration of a PINK1 input signal.

<p style="text-align:center">TABLE OF CONTENTS</p>

LIST OF FIGURES

LIST OF ABBREVIATIONS

ACT – Activating domain

AFU – Arbitrary fluorescence units

ATP – Adenosine triphosphate

CCCP – Carbonyl cyanide m-chlorophenyl hydrazone

CD – C-terminal domain

Det. – Detectable

EGF – Epidermal growth factor

EGFR – Epidermal growth factor receptor

FIS1 – Fission, mitochondrial 1

FKBP – F506-binding protein domain

fl-PINK1 – Full-length PINK1

FRB – FKBP-rapamycin-binding domain

GAB1 – GRB2 associated binding protein 1

IBR – In-between ring domain

Init. – Initial

IR – Insulin receptor

IRS – Insulin receptor substrate

Mito. – Mitochondrial

mKO2 – Monomeric kusabira orange

mNG – mNeonGreen

MOM – Mitochondrial outer membrane

mTOR – Mechanistic target of rapamycin

MTS – Mitochondrial targeting sequence

MtTether – Mitochondrial tether

Multi. – Multiplier

ND – N-terminal domain

PI3K – Phosphoinositide 3-kinase

PINK1 – PTEN-inducible kinase 1

PIP3 – Phosphatidylinositol (3,4,5)-triphosphate

PTEN-L – Phosphatase and tensin homolog long isoform

pUb – Phosphorylated ubiquitin

px – pixel

Rapalog – Rapamycin analog

REP – Repressive domain

RING0 – Really interesting new gene domain 0

RING1 – Really interesting new gene domain 1

RING2 – Really interesting new gene domain 2

Thresh. – Threshold

TM – Transmembrane domain

TOM – Translocase of the outer membrane

TOM20 – Translocase of the outer membrane 20

Ub – Ubiquitin

UBL – Ubiquitin-like domain

USP30 – Ubiquitin-specific protease 30

CHAPTER 1

A PINK1 input threshold arises from positive feedback in the PINK1/Parkin mitophagy

decision circuit

1.1 Abstract

Mechanisms that prevent accidental activation of the PINK1/Parkin mitophagy circuit on healthy mitochondria are poorly understood. On the surface of damaged mitochondria, PINK1 accumulates and acts as the input signal to a positive feedback loop of Parkin recruitment, which in turn promotes mitochondrial degradation via mitophagy. However, PINK1 is also present on healthy mitochondria where it could errantly recruit Parkin and thereby activate this positive feedback loop. Here, we explore emergent properties of the PINK1/Parkin circuit by quantifying the relationship between mitochondrial PINK1 concentrations and Parkin recruitment dynamics. We find that Parkin is recruited to mitochondria only if PINK1 levels exceed a threshold and then only after a delay that is inversely proportional to PINK1 levels. Furthermore, these two regulatory properties arise from the input-coupled positive feedback topology of the PINK1/Parkin circuit. These results outline an intrinsic mechanism by which the PINK1/Parkin circuit can avoid errant activation on healthy mitochondria (**Figure 1.1**).

1.2 Introduction

Mitochondrial polarization is critical for mitochondrial function and is a key indicator of mitochondrial health[1–4]. Cells maintain a healthy pool of mitochondria by degrading depolarized mitochondria via mitophagy (mitochondrial autophagy)[1,5–9]. A core molecular circuit mediating the mitophagy decision involves PINK1, a mitochondrial kinase, and Parkin, a cytoplasmic E3 Ubiquitin ligase[10]. While PINK1 is constitutively recruited to the mitochondrial outer membrane (MOM), polarization-dependent degradation keeps PINK1 levels low on healthy, polarized, mitochondria[6,7]. Mitochondrial depolarization prevents this degradation and leads to accumulation of PINK1 on the MOM over time[6,7]. Upon PINK1 accumulation, positive feedback in the

PINK1/Parkin circuit leads to extensive labeling of the mitochondrial surface with phospho-S65 Ubiquitin (pUb) and to pUb-dependent recruitment of downstream mitophagy machinery[10–12].

Positive feedback in the PINK1/Parkin circuit occurs through a series of steps (**Figure 1.2A**): PINK1 phosphorylates mitochondrial Ubiquitin, pUb recruits autoinhibited Parkin to the MOM, PINK1 phosphorylates Parkin's Ubiquitin-like (UBL) domain to activate Parkin, and activated Parkin deposits new Ubiquitin on proteins at the MOM[10,13–23]. Newly deposited Ubiquitin can then be phosphorylated by PINK1, starting new rounds of amplification[10,24]. Together, these steps constitute the positive feedback topology of the PINK1/Parkin circuit, where PINK1 provides an input signal and positive feedback occurs via Parkin's ubiquitin ligase activity[11].

While positive feedback in the PINK1/Parkin circuit enables rapid and robust signal amplification on depolarized mitochondria[10,25], healthy mitochondria are somehow able to tolerate constant recruitment and release of PINK1[6,7] as well as transient depolarization[26,27] without triggering runaway positive feedback. A range of theoretical regulatory mechanisms have been proposed for how the PINK1/Parkin circuit could avoid such errant activation[11,13,24,26,28–31]. One intriguing hypothesis is that mitochondrial PINK1 concentrations may need to exceed some threshold value to provoke a circuit activation response (**Figure 1.2B**)[29,32]. However, investigation of such emergent behaviors has been limited by a lack of techniques for holding mitochondrial PINK1 concentrations steady while the corresponding circuit response is measured[26].

Here, we investigated whether emergent regulatory behaviors exist in the PINK1/Parkin positive feedback circuit. We used a synthetic circuit approach to quantitatively map the relationship between discrete mitochondrial PINK1 concentrations and Parkin recruitment dynamics. This input-response mapping revealed two regulatory properties: a PINK1 input threshold for circuit activation fate and a PINK1 input-reciprocal delay for circuit activation

3

timing. Further mutational and mathematical evaluation revealed that these two regulatory properties arise intrinsically from the positive feedback topology of the PINK1/Parkin circuit. Together, our results demonstrate a mechanism by which the PINK1/Parkin circuit could avoid unchecked positive feedback activation.

1.3 Results

To evaluate emergent behavior of the PINK1/Parkin positive feedback circuit, we adapted a previously described minimal synthetic PINK1/Parkin circuit[6,33] for four-color quantitative microscopy. The minimal synthetic circuit was comprised of 1) fluorescently-labeled Parkin and 2) fluorescently-labeled PINK1 which could be targeted to fluorescently-labeled mitochondria using a rapalog-(rapamycin analog)-induced recruitment system[6,33–35] (**Figure 1.2C-D**). All components were expressed in HeLa cells, which do not express endogenous Parkin[7,36] (methods). This synthetic circuit approach enabled us to evaluate emergent properties of the circuit by quantifying the relationship between relatively stable circuit inputs (PINK1 concentration on mitochondria) and resulting circuit activation (Parkin localization to mitochondria) in an isolated setting.

1.3.1 Internally tagged Parkin probe.

Parkin relocalization from the cytoplasm to phospho-S65 Ubiquitin (pUb) on the mitochondria is an established method for measuring PINK1/Parkin circuit activation[6]. To track PINK1/Parkin circuit activation, we optimized a fluorescent tagging approach for Parkin. Traditionally used N-terminal tags are known to perturb Parkin's conformational stability[37] and could affect Parkin's mitophagy activity. Parkin's N-terminal ubiquitin-like (UBL) domain is the phosphorylation site for PINK1. Phosphorylated UBL (pS65-UBL, pUBL) plays a critical role in

4

unlocking the catalytic activity of Parkin[19,20,23]. Thus, we reasoned that a conformational destabilization of N-terminally tagged Parkin[37] could cause a functional defect in Parkin either by affecting PINK1's ability to recognize the UBL domain or by affecting the pUBL domains' role in unlocking Parkin's catalytic activity. In agreement with this prediction, we found that Parkin, N-terminally tagged with monomeric Kusabira-Orange2 (mKO2), displayed reduced recruitment to and degradation of chemically depolarized mitochondria (**Figure A.1A-H** and **Figure A.2A-E**, Nterm-M1).

Upon further investigation, we found that Parkin's N-terminal $NH3^+$ group appears to engage in a conserved salt bridge with E16 (**Figure A.1I-P**)[38] that would be disrupted by N-terminal tagging. Mutation of E16 of untagged Parkin to alanine (Untagged-E16A) decreased Parkin recruitment to and degradation of chemically depolarized mitochondria (**Figure A1.Q**; **Figure A.2A-E**), suggesting a functional impact of the predicted salt bridge. Furthermore, a commonly used substitution in N-terminally tagged Parkin of M1 to leucine (Nterm-M1L) – for removing a cryptic translation start site – appeared to display decreased Parkin recruitment and mitochondrial degradation compared to Nterm-M1 (**Figure A.1A-H** and **Figure A.2A-E**, p-value not calculated), suggesting that Parkin's function is sensitive to even small packing changes at its N-terminus. These observations suggest that N-terminal tags may disrupt the structural stability of Parkin's UBL domain and prompted us to investigate alternative internal tagging locations.

We identified an internal Parkin tagging site, between A92 and G93, that is: 1) within a disordered[19,20] and non-conserved linker region (**Figure A.1D**), and 2) distinct from other previously described internal-tagging sites which alter Parkin relocalization dynamics[22]. We found that Parkin, internally tagged with mKO2 at A92, displayed untagged-like mitophagy activity (**Figure A.1E-H** and **Figure A.2A-E**). Based on these results, we chose to use internally tagged

Parkin as both a component of—and activation reporter for—our minimal synthetic circuit (**Figure 1.2C**).

1.3.2 Stable PINK1 recruitment to mitochondria.

Traditional mitochondrial depolarization methods cause PINK1 accumulation over time and are therefore not capable of producing stable mitochondrial PINK1 levels[26]. To control and quantify PINK1 concentrations on mitochondria, we optimized a previously described rapalog-induced PINK1 recruitment system[6,33,39,40] for quantitative microscopy. An FRB/FKBP/rapalog system[34,35] was used to control dimerization between mNeonGreen (mNG) tagged PINK1 and a SNAP-tagged mitochondrial tether (MtTether; **Figure 1.2C-D**; **Figure A.3A**; methods). Upon rapalog treatment, this allows relocalization of PINK1 from the cytoplasm to mitochondria in live cells to be monitored (**Figure 1.2E-G**; methods). Rapalog-induced PINK1 localization to mitochondria was reasonably stable over time within our measurement precision (**Figure 1.2F-I**; **Figure A.3B**). Notably, PINK1 and MtTether expression was designed to enable a range of mitochondrial PINK1 concentrations across cells in each experiment (**Figure A.3C**; methods). We verified: that PINK1 mediates Parkin recruitment to and degradation of mitochondria (**Figure A.3D**)[6,33], that PINK1's role requires its kinase activity (**Figure A.3E**)[33], and that rapalog treatment did not exhibit off-target effects on mTOR signaling in our system (**Figure A.3F**). Consistent with previous reports, activation of the circuit did not cause mitochondrial depolarization[33]. This PINK1 and MtTether rapalog-induced recruitment system enabled us to stably direct PINK1 to the mitochondria in our minimal PINK1/Parkin synthetic circuit.

1.3.3 Quantification of synthetic circuit dynamics.

To define the behavior of the minimal PINK1/Parkin synthetic circuit, we developed a quantification approach to evaluate the relationship between mitochondrial PINK1 levels and Parkin recruitment at single-cell resolution. Initial observations revealed heterogenous circuit dynamics where cells with high mitochondrial PINK1 underwent Parkin relocalization to mitochondria (**Figure 1.2F**) while cells with low mitochondrial PINK1 did not (**Figure 1.2G**). We quantified these circuit dynamics for each cell by tracking mitochondrial PINK1 concentration (via mean PINK1 intensity) and Parkin recruitment (via correlation of Parkin and MtTether intensities) (**Figure 1.3H-I**; methods) over time. From this data, we calculated single-cell estimations for 1) the mean concentration of PINK1 on mitochondria after rapalog treatment, 2) the maximal Parkin recruitment response, and 3) the time of Parkin recruitment (**Figure 1.2H-I**; methods). This triplet of metrics summarized the behavior of the minimal PINK1/Parkin synthetic circuit.

1.3.4 A PINK1 concentration threshold controls PINK1/Parkin circuit activation.

To examine emergent behavior of the PINK1/Parkin synthetic circuit, we first evaluated circuit activation fates as a function of PINK1 mitochondrial concentration. Plotting the mean concentration of PINK1 on mitochondria against the associated maximal Parkin recruitment responses of individual cells revealed two distinct response populations (**Figure 1.3A**, points). Specifically, cells with higher mitochondrial PINK1 concentrations underwent Parkin recruitment while cells with lower mitochondrial PINK1 concentrations did not undergo Parkin recruitment (**Figure 1.3A**, points). These two populations were distinguished by a sharp inflection point along the PINK1 concentration axis (**Figure 1.3A**, sliding median). Because the synthetic circuit in these cells was given time to reach a stable response state, existence of these two populations supports

the existence of a PINK1 concentration threshold that mitochondrial PINK1 levels must surpass to detectably recruit Parkin. This "PINK1 input threshold" was quantified as the PINK1 concentration that best separated the two populations (**Figure 1.3A-B**; methods). Finally, we checked that cells lacking detectable Parkin recruitment to mitochondria also lacked detectable levels of mitochondrial pUb (**Figure A.3G-H**) and that the PINK1 concentration threshold was observed using an alternative Parkin recruitment metric (**Figure A.3I-J**). These results suggest that our conclusions are robust with respect to both potential detection limitations and quantification approaches. Taken together, our work shows that the minimal PINK1/Parkin synthetic circuit exhibits a PINK1 concentration threshold for circuit activation.

To further examine emergent behavior of the synthetic circuit, we evaluated circuit activation timing as a function of PINK1 mitochondrial concentration. While a delay for detectable Parkin recruitment is readily observed in depolarization-based assays and can be decreased by overexpressing PINK1[6], the exact relationship of this delay to PINK1 levels is unknown. Plotting the mean concentration of PINK1 on mitochondria against the time of Parkin recruitment of individual cells revealed an inverse relationship that was well fit by a hyperbolic curve (**Figure 1.3C**, R^2=0.886). Specifically, this analysis revealed an "input-reciprocal delay" for Parkin recruitment: doubling the amount by which PINK1 mitochondrial concentration exceeds the PINK1 input threshold will halve the time required for Parkin recruitment. The input-reciprocal delay relationship was described by the numerator of the fit hyperbolic curve, the "delay multiplier" (**Figure 1.3C**). Both the input-reciprocal delay behavior, as well as the PINK1 input threshold behavior, was recapitulated by fixed-cell time series which had the advantage of allowing quantification from a greater number of cells (**Figure 1.3D**; **Figure A.3K-L**). Furthermore, by leveraging both cell-to-cell heterogeneity in Parkin expression levels (**Figure**

A.4A-D) and an ultralow strength promoter for Parkin expression (**Figure A.4E-I**), we showed that the observed PINK1 input threshold and input-reciprocal delay behaviors were robust across a wide range of Parkin expression levels. Finally, we found that, within the measurement accuracy of our instruments, recruitment of PINK1 and Parkin to mitochondria was spatially and temporally uniform (**Figure A.5**), suggesting that the observed Parkin recruitment delay behavior does not arise from Parkin recruitment seeding at one point and spreading at a PINK1 concentration-dependent rate. Together, the PINK1 input threshold and input-reciprocal Parkin recruitment delay suggest a "two-factor" regulatory paradigm for activation of the PINK1/Parkin circuit where circuit activation is controlled by the amount of PINK1 and the duration of the PINK1 signal.

1.3.5 PINK1 autophosphorylation is not required for emergent behavior.

To explore how the observed circuit behaviors could arise, we first evaluated whether PINK1 autophosphorylation is necessary for producing the PINK1-input threshold and/or input-reciprocal delay. PINK1 autophosphorylation at the key S228 locus (**Figure 1.4A-B**) occurs in *trans* and increases PINK1's kinase activity for both Parkin and Ubiquitin[28,41,42]. We reasoned that such a requirement for two PINK1 molecules to interact could produce a form of threshold or delay behavior. Hence, we made use of PINK1 S228A (non-phosphorylatable) and S228D (phospho-mimetic and non-phosphorylatable) mutants[28,41,42] in our minimal PINK1/Parkin synthetic circuit (**Figure 1.4B**; **Figure A.6A**).

We found that the S228A PINK1 mutation caused an increase in both the PINK1 input threshold and delay multiplier, while the S228D mutation caused a decrease in both circuit properties (**Figure 1.4C-D**; **Figure A.6B**). S228A PINK1's retained ability to recruit Parkin (**Figure A.6B**) suggests that autophosphorylation of PINK1 at S228 is not necessary for recruitment of Parkin in our system. The opposing directions of S228A- and S228D-dependent

changes (**Figure 1.4C-D**) support previous observations that PINK1 autophosphorylation at S228 promotes efficient Parkin recruitment[28,41,42]. The two mutants define extremes for the range of how autophosphorylation at S228 can affect circuit behavior in our system (**Figure 1.4C-D**). However, the existence of quantifiable PINK1 input threshold and input reciprocal delay behaviors at these extremes (**Figure 1.4C**) shows that S228 phosphorylation is not necessary for producing these behaviors. Taken together, these data demonstrate that PINK1 S228 autophosphorylation in *trans* may tune the PINK1 input threshold and the input-reciprocal delay for Parkin recruitment yet is not necessary for producing these circuit behaviors.

1.3.6 Parkin activation dynamics tune PINK1 input threshold behavior.

To further explore how the observed circuit behaviors could arise, we next used previously characterized Parkin mutants (**Figure 1.5A**) to rationally perturb Parkin activation dynamics (**Figure 1.5B**; **Figure A.6A**). Parkin becomes catalytically active and enables positive feedback in the PINK1/Parkin circuit by undergoing a series of dramatic pUb-dependent and PINK1-dependent domain rearrangements (**Figure 1.5B**)[19–23,43,44]. Initially cytoplasmic Parkin exists in an autoinhibited conformation where both the S65 PINK1-phosphorylation site in the UBL domain, the C431 catalytic residue of the RING2 domain are masked, and where the UBCH7 E2 ubiquitin ligase binding site is blocked by the UBL and the REP (repressive) domains (**Figure 1.5B**, left)[21,23]. First, Parkin binding to pUb causes a conformational change that dislodges the UBL domain, revealing the S65 PINK1 phosphorylation site (**Figure 1.5B**, left)[23]. If the UBL domain is not phosphorylated, it can allosterically compete with pUb for binding[23]. Once phosphorylated, the pUBL, with assistance from the ACT (activating) domain, competes for binding with and displaces the RING2 domain and the REP domain to fully activate the E3 ubiquitin ligase activity of Parkin (**Figure 1.5B**, right)[19,20]. Because these domain rearrangements are defined by either allosteric

competition or direct competition for binding (pUb vs UBL and pUBL vs RING2 respectively), the dynamics of Parkin activation can be rationally altered by introducing mutations that affect the competition and influence the proportion of time spent in each conformation[22,23,44,45].

We introduced five Parkin mutations – S65A, K161N, R104A, W403A, or N273K – in our synthetic circuit to alter the kinetics of these domain rearrangements. S65A blocks PINK1's ability to phosphorylate Parkin's UBL domain[18]. S65A, K161N, and R104A are each expected to decrease Parkin's catalytic activity by reducing the ability of Parkin's phosphorylated UBL domain to displace and free Parkin's catalytic RING2 domain[19–21,45] (**Figure 1.5B**; **Figure A.6A**). Conversely, W403A is expected to increase Parkin's catalytic activity by weakening autoinhibitory REP and RING2 interactions and thus allowing Parkin to spend a higher proportion of time in its active conformation[16,19,21–23,44,45] (**Figure 1.5B**; **Figure A.6A**). (We note that while unphosphorylated W403A Parkin exhibits some baseline catalytic activity[16,21,22,45] [**Figure 1.5B**, inset], phosphorylation of W403A Parkin by PINK1 is still required to fully activate the mutant[44]). Finally, N273K increases Parkin's affinity for pUb by 10-fold by altering allosteric competition between UBL and pUb binding[22,23] (**Figure 1.5B**; **Figure A.6A**).

First, S65A and K161N mutations completely blocked Parkin recruitment (**Figure 1.5C**; **Figure A.6C-D**). The lack of recruitment of both S65A Parkin and K161N Parkin supports prior observations that positive feedback via Parkin activation is critical for activation of the PINK1/Parkin circuit[11,19,22,43]. Second, the R104A mutation produced an increased PINK1 input threshold and an increased delay multiplier (**Figure 1.5C**; **Figure A.6C-D**), while the activating W403A mutation produced a decrease in both circuit properties (**Figure 1.5C**; **Figure A.6C-D**). These opposing effects of the R104A and W403A suggest that Parkin's activity contributes to generating threshold and delay behaviors in the positive feedback circuit.

Finally, and most interestingly, the N273K mutation decreased the PINK1 input threshold but did not affect the delay multiplier (**Figure 1.5C**; **Figure A.6C-D**). This decreased PINK1 input threshold (**Figure 1.5C**) suggests that the strength of Parkin's association with pUb is a critical contributing factor to the PINK1 input threshold behavior (intuitively, increasing Parkin's affinity for pUb leads to lowered input threshold). The unchanged delay scaler (**Figure 1.5C**) demonstrates that the PINK1 input threshold and the input-reciprocal delay can be modulated independently, a property that was not initially obvious. The observation that the delay multiplier was affected by mutations altering Parkin's activity (W403A and R104A) but not by N273K (**Figure 1.5C**) suggests that the timing of circuit activation is primarily influenced by positive feedback in the PINK1/Parkin circuit. Taken together, these results suggest that the PINK1 input threshold is tuned by multiple factors—including Parkin's binding affinity for pUb and Parkin's ability to drive positive feedback—while the circuit's activation delay is dominated by the effect of positive feedback.

To explore the functional interplay between PINK1 activity and Parkin activity, we assessed whether the hyperactive S228D PINK1 mutant could rescue activity defects in the S65A, K161N, or R104A Parkin mutants. The lack of S65A and K161N Parkin recruitment was not rescued by S228D PINK1 (**Figure A.6E**) suggesting a profound activity defect in these Parkin mutants. Conversely, WT and R104A Parkin's PINK1 input threshold and delay scaler were both decreased for the S228D PINK1 condition with R104A Parkin retaining a higher PINK1 input threshold and delay multiplier compared to WT Parkin (**Figure 1.5D**; **Figure A.6E-F**). Thus, PINK1 and Parkin activities cooperate to tune the PINK1 input threshold and delay multiplier. Because each round of positive feedback in the PINK1/Parkin circuit requires contributions by

both PINK1 and Parkin (**Figure 1.2A**), our results suggest that the identified behaviors arise from the circuit's positive feedback topology.

1.3.7 Input-coupled positive feedback is sufficient to produce two-factor authentication.

To test whether the positive feedback topology of the PINK1/Parkin circuit is sufficient to produce the observed PINK1 input threshold, we investigated mathematical models based on the circuit. A defining feature of the PINK1/Parkin circuit is that it has an "input-coupled" positive feedback topology: the input is continually required for positive feedback, and increased input increases the net rate of feedback. A "minimal" model with this circuit topology is the conversion of a substrate X to pX that requires the input of an enzyme E and pX itself (**Figure 1.6A**). Here, E abstracts the enzyme PINK1, X abstracts the pool of free Ub and free Parkin, and pX abstracts the pools of pUb and pParkin.

The minimal model can be described by a simple ordinary differential equation and solved analytically (**Figure 1.6A**; **Appendix B**). In striking agreement with our experiments, this model displays both a defined input-threshold, below which the circuit will not activate, and a hyperbolic law inversely relating input concentration and delay for pX to reach an arbitrary minimum detection level pX_{det} (e.g., experimentally by our microscope, or biologically by downstream mitophagy components) from its initial level pX_{init} (**Figure 1.6B-C**, analytical curve; **Figure A.7A-E**; **Appendix B**; methods).

We stress-tested behaviors of the minimal model. First, we found that the input threshold and input-reciprocal delay behaviors emerged from a broad class of generalized models for input-coupled positive feedback, including a detailed model of the PINK1/Parkin circuit with free, bound, and phosphorylated states of both Ub and Parkin (**Figure A.7F-G**; **Appendix B**). Second,

experimentally observed circuit response heterogeneity could be qualitatively recapitulated by varying single-cell parameters in the minimal mathematical model (**Figure 1.6B-D**, points; methods). Third, experimentally observed effects of Parkin mutants could be predicted from the analytical expression of threshold and delay (**Figure 1.6E**). Finally, we investigated responses of the circuit to transient input fluctuations using numerical simulations (experimentally, the rapalog system is poorly suited to test these properties; dissociation half-life, t1/2 > 2hours). These simulations demonstrated that the emergent circuit threshold and delay behaviors—integrating the level and duration of a PINK1 input—can provide a mitophagy fate decision mechanism to discern between "false alarms" and severe mitochondrial damage (**Figure 1.6F**). These simulation results agree with published data showing that circuit activation is readily reversed upon mitochondrial repolarization (**Figure 1.6F**, middle)[7,26,33]. Together these analyses show that the input-coupled positive feedback topology of the PINK1/Parkin pathway is sufficient to generate the regulatory behaviors of input threshold and input-reciprocal circuit activation delay—a conclusion that was not immediately obvious from our initial understanding of the circuit.

1.4 Discussion

This study reveals an intrinsic regulatory mechanism by which the PINK1/Parkin positive feedback circuit can avoid errant activation. We used a minimal synthetic circuit approach to directly map circuit inputs (mitochondrial PINK1 concentration) to circuit activation responses (Parkin recruitment) at single-cell resolution. This approach revealed two modes of regulation: 1) that circuit activation can occur only when mitochondrial PINK1 concentrations exceed a threshold value; and 2) that, once above this PINK1 input threshold, appreciable circuit activation is delayed by a time inversely proportional to the mitochondrial PINK1 concentration. Furthermore, a combination of mutational and mathematical analyses revealed that these two

regulatory behaviors arise from input-coupled positive feedback, a defining feature of the PINK1/Parkin positive feedback circuit topology.

Prior work has proposed mechanisms that could give rise to input threshold and input reciprocal delay behaviors in the PINK1/Parkin positive feedback circuit[11,13,24,26,28–31]. Initial interpretation of the circuit's topology as a series of feedforward loops led to speculation that a feedforward-based delay could prevent circuit activation by transient PINK1 association[11,24,26]. Recent work has further speculated that a relationship between PINK1 levels and the probability to activate this feedforward mechanism could also produce a PINK1 input threshold[29,32]. Here, we propose input-coupled positive feedback as an alternative conceptual framework for understanding the role of positive feedback in the circuit's topology. Intuitively, input-coupled positive feedback reframes the serialized feedforward loops into a positive feedback format. Thus, our findings that the PINK1 input threshold and input reciprocal delay exist and that they emerge from the circuit's topology confirm prior intuition about emergent behaviors of the PINK1/Parkin circuit.

Our mathematical modeling suggests the input threshold and input reciprocal delay behaviors are intrinsic properties of the PINK1/Parkin circuit's organization. However, contextual factors could affect whether an input threshold may be experimentally observable for the endogenous circuit. Activation of the endogenous circuit by mitochondrial depolarization is promoted both by secondary depolarization effects (reactive oxygen species formation, ATP depletion)[46–48] and by full-length PINK1's (fl-PINK1) localization to the TOM (translocase of the outer membrane) complex[13,28,33,49]. In contrast, the synthetic circuit lacks both sensitizing effects because its activation does not involve mitochondrial depolarization[33] and because the PINK fusion is not expected to interact with the TOM complex[33]. The higher sensitivity of the endogenous circuit is reflected in the low, nearly undetectable, expression of endogenous PINK1

(**Figure A.8A**). This low expression of endogenous fl-PINK1, coupled with a current lack of techniques for holding fl-PINK1 levels steady on depolarized mitochondria[26], hamper input-response mapping for the endogenous circuit. Evaluation of circuit threshold and delay behaviors in the endogenous context may require the development of new single-molecule analysis or *in-vitro* reconstitution techniques.

PINK1 autophosphorylation in *trans* at S228 is not required for generating either the PINK1 input threshold or the input reciprocal delay behaviors in our synthetic circuit. Furthermore, in the synthetic circuit, S228A PINK1 can recruit Parkin, suggesting that S228A PINK1 retains some kinase activity. This conclusion is supported by previous findings that *Tribolium castaneum* Parkin, with the equivalent S205A mutation, retains some kinase activity for Parkin's UBL[28]. However, previous work has also shown that S228A fl-PINK1 is not capable of recruiting Parkin or generating pUb in depolarization-based assays[28,49]. One possible explanation for this discrepancy is that the relatively high expression level of PINK1 in the synthetic circuit could compensate for the activity defect of S228A PINK1. Additionally, it is possible that the focal concentration of fl-PINK1 may be limited by the 2:1 stoichiometry of fl-PINK1's interaction with the TOM complex on depolarized mitochondria[49,50]. The combined kinase activity of just two S228A (or unphosphorylated) fl-PINK1 molecules bound to a single TOM complex might be insufficient to overcome the PINK1 input threshold on a local scale. Thus, PINK1 autophosphorylation could play a role in overcoming the circuit's PINK1 input threshold on depolarized mitochondria despite not being necessary in the synthetic circuit.

During the early stages of this study, we found that N-terminally tagged Parkin displays a functional deficit. This finding expands upon previous work that showed N-terminal tags destabilize the autoinhibition of Parkin[37]. Our results further show that the apparent functional

defect of N-terminally tagged Parkin, may be due to structural instability in the UBL domain induced by disruption of a predicted salt bridge involving the UBL's N-terminal NH3^{+} group. While disruption of the predicted salt bridge would be unavoidable if an N-terminal tag were used, it may be possible for future work to compensate for this structural destabilization using linker optimization based on internal UBL domains or based upon insect Parkin which has an N-terminal extension[51]. To address the concerns of N-terminal tag effects on Parkin, we identified a site at A92 as an alternative tagging site that avoids the functional deficit associated with N-terminal tags. However, because we only optimized the A92 tagging site for use with an mKO2 fluorescent tag, further work will be required to explore whether the same internal tagging site can be used with other epitope or fluorescent tags. Together these results suggest that care should be taken in future studies when choosing a tagging approach for Parkin or for other proteins with N-terminal UBL domains.

Our results suggest that PINK1 activity and Parkin activation dynamics play a large role in tuning the emergent behaviors of the PINK1/Parkin circuit. Antagonistic enzymes could also contribute to tuning these behaviors. Indeed, we found that pharmacological inhibition of the mitochondrial deubiquitinase USP30[11,52–55] slightly decreased both the PINK1 input threshold and delay multiplier (**Figure A.8B-E**). The magnitude of the observed effect is consistent with prior work showing that USP30 knockout only modestly increases Parkin recruitment to chemically depolarized mitochondria[13] possibly due to USP30's low activity for pUb[31]. This low activity for pUb has prompted speculation that USP30 may tune the PINK1/Parkin pathway by regulating basal ubiquitin levels and not by directly counteracting the PINK1/Parkin positive feedback circuit[13]. We note that our findings (**Figure A.8B-E**) do not provide clear insight into the mechanism by which USP30 modulates PINK1/Parkin circuit activation. Future work will be

required to explore whether USP30 affects the PINK1/Parkin circuit by regulating basal ubiquitin levels, by directly antagonizing circuit activation, or both. Regardless, the presence of a tuning effect for USP30 inhibition suggests that modulation of emergent behaviors by antagonistic factors is at least possible. Other antagonistic factors of interest include cytoplasmic deubiquitinases[56] and the putative Ubiquitin phosphatase PTEN-L[57]. Further exploration of how such enzymatic antagonists tune circuit behaviors may aid in identifying pharmacological approaches for modulating PINK1/Parkin circuit dynamics.

Finally, in addition to producing noise-tolerant circuit activation profiles, input-coupled positive feedback intrinsically provides control over where amplification can occur. For example, because the presence of input is required to maintain positive feedback, PINK1/Parkin circuit activation is not expected to spread to healthy mitochondria where PINK1 is not present at activating levels[3,5,6,58]. This contrasts with a more classic form of positive feedback in which the input is decoupled from the feedback rate and for which spatially constrained activation may be lost without additional considerations[59,60]. Beyond mitophagy, there are other systems where input-coupled positive feedback may operate to produce robust local responses. In EGF receptor (EGFR) signaling, an EGFR-driven positive feedback loop involving GAB1, PI3K and PIP3 matches the topology of an input coupled positive feedback circuit[61,62]. A similar positive feedback loop also exists for insulin receptor (IR) signaling via IRS, PI3K, and PIP3[62]. Taken together, our work motivates future studies into how input-coupled positive feedback may contribute to cellular decisions by balancing signal amplification sensitivity, noise tolerance, and spatial cues.

1.4.1 Limitations of the study

In summary, this study has several limitations. To hold mitochondrial PINK1 levels steady over time, and to facilitate live-cell imaging, a synthetic circuit composed of overexpressed

components was used. Further study of the physiological relevance of the PINK1 input threshold and input reciprocal delay may require the development of novel single-molecule imaging or *in vitro* reconstitution methodologies. Additionally, the slow dissociation rate of the PINK1-MtTether interaction in the synthetic circuit prevented us from examining the circuit's response to pulses of mitochondrial PINK1. The use of an optically controlled dimerization system could enable future work to examine circuit responses to transient stimuli and to explore potential hysteresis behaviors of the circuit.

1.5 Figures
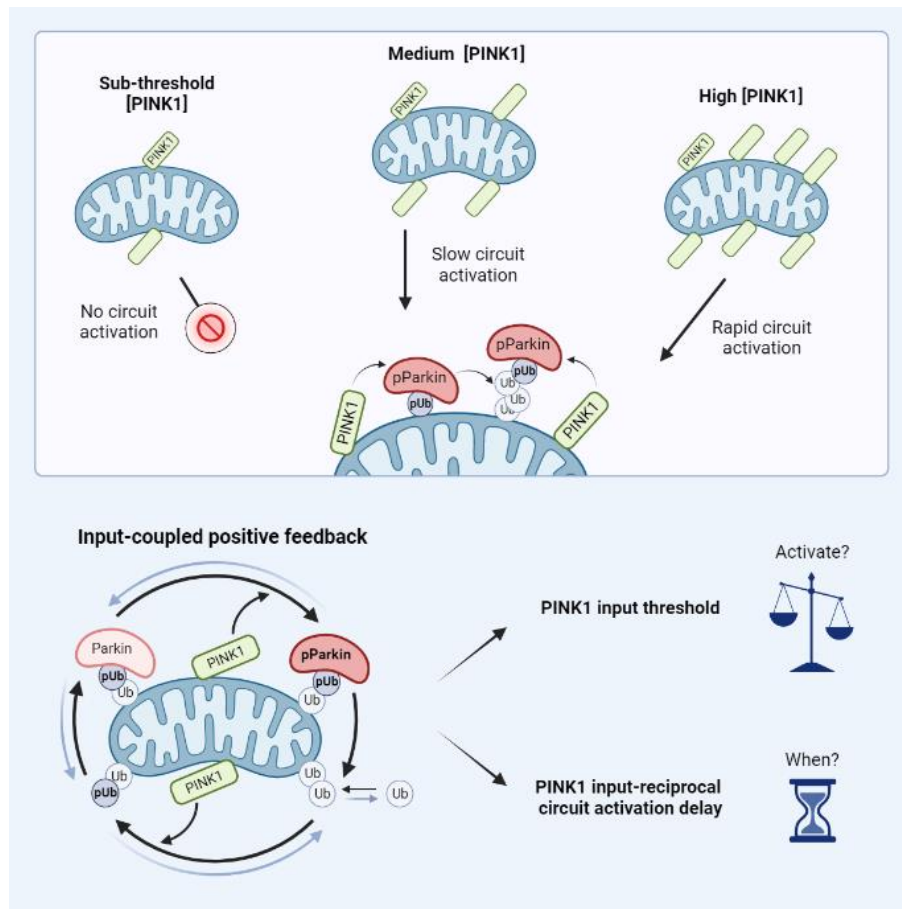
Figure 1.1: Graphical abstract
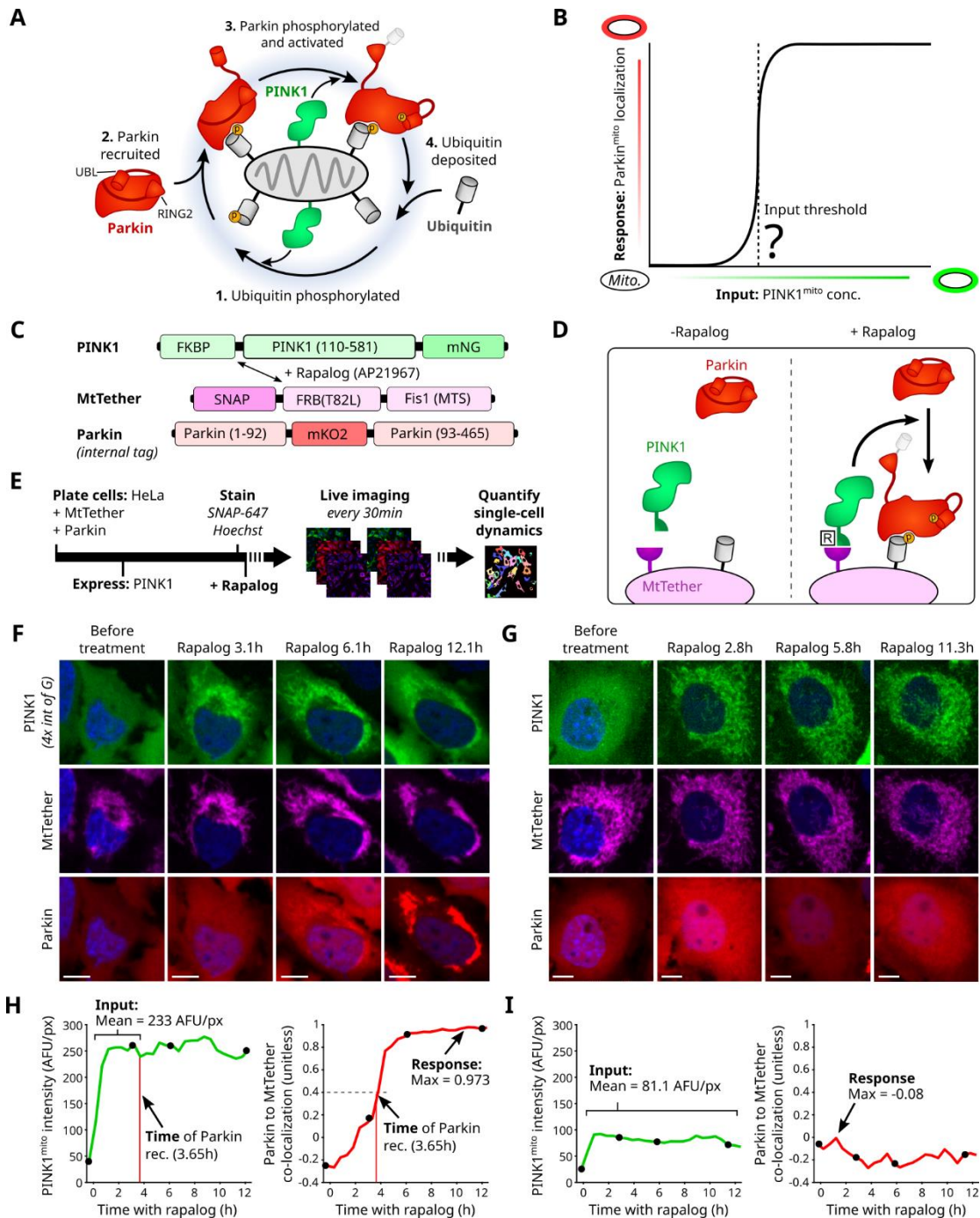
Figure 1.2: Quantification of input-to-output responses for a minimal PINK1/Parkin synthetic circuit. (A) Cartoon of PINK1/Parkin positive feedback loop. Yellow circles: phosphorylation sites. Conformational changes of activated Parkin's UBL (ubiquitin-like) and catalytic RING2 domains shown. Yellow circles: phosphorylation sites. **(B)** Hypothetical input-response relationship (curve) illustrating a PINK1 input threshold for circuit activation (vertical dashed line). Inputs: discrete mitochondrial PINK1 concentrations, held stable over time. **(C-D)** PINK1/Parkin synthetic circuit using (*Figure caption continued on the next page*)

(*Figure caption continued from the previous page*) rapalog-induced PINK1^{mito} recruitment. Mitochondrial targeting sequence (MTS) of PINK1, amino acid 1-109, removed. T82L: mutation required for rapalog binding. (**E**) Live-cell imaging approach. Rapalog treatment: 200nM. SNAP-647: fluorescent SNAP ligand for far-red imaging of MtTether (methods). Bar length not to scale. (**F-G**) Representative timelapse images of cells with (F) or without (G) Parkin^{mito} recruitment in response to induced PINK1^{mito} recruitment. Scale bars: 10um. Relative intensity visualization range noted in (F). (**H-I**) Quantification of circuit input (mean PINK1^{mito} concentration), circuit response (max Parkin^{mito} recruitment), and the time of Parkin^{mito} recruitment for cells in (F-G). AFU: arbitrary fluorescence units. Co-localization: foreground intensity correlation (Pearson, methods). Black points: timepoints in (F-G).
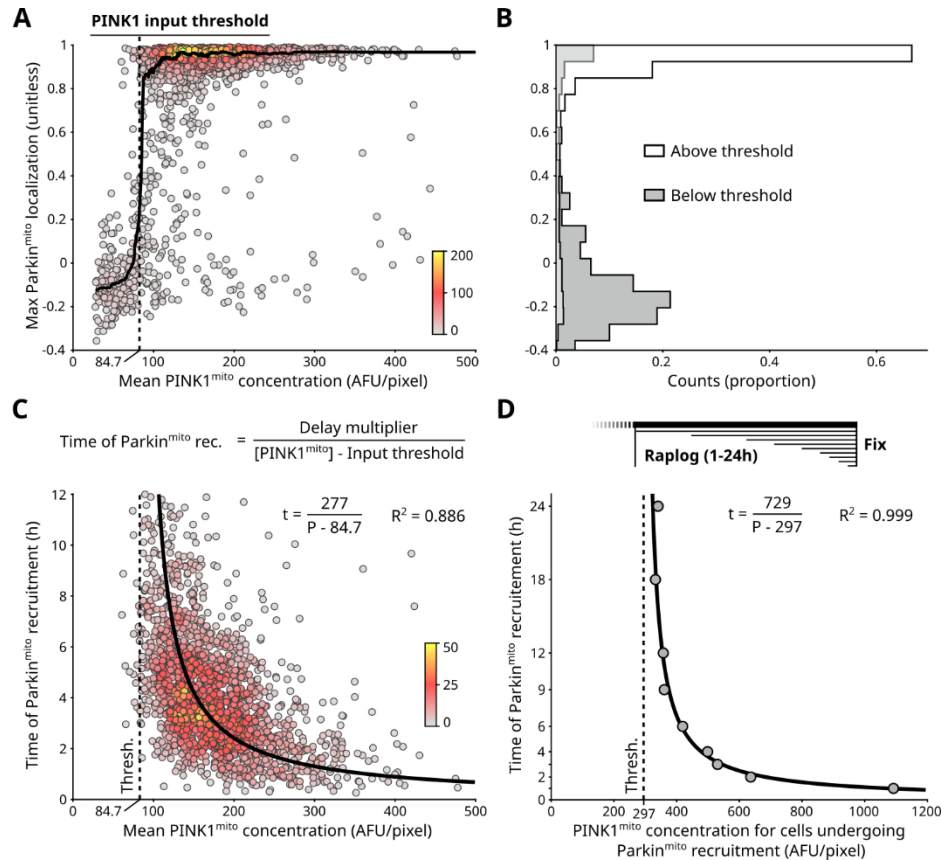
Figure 1.3: A PINK1 concentration threshold controls activation of the PINK1/Parkin circuit. (**A**) Single cell measurements for circuit input (PINK1^{mito} concentration) and circuit response (Parkin^{mito} localization) for n=1987 cells (**Figure 1.2H-I**; methods). Points: individual cells, colored by local point density (number of nearby points, methods). Solid line: sliding median. PINK1 input threshold: PINK1^{mito} concentration required for Parkin^{mito} recruitment (methods). (**B**) PINK1 input threshold separates cells with and without Parkin^{mito} recruitment. (**C**) Timing of Parkin^{mito} recruitment has a reciprocal relationship to PINK1^{mito}. Points: n=1676 cells with Parkin^{mito} recruitment from (A) (**Figure 1.2H**; methods), colored by local point density. General equation of reciprocal relationship shown. Delay multiplier numerator defines hyperbolic relationship. Fitted hyperbolic curve and R^2 value are shown. Brackets: concentration. (**D**) PINK1 input threshold (dashed line) and timing hyperbola (solid line) quantified using analysis of fixed cells following various durations of rapalog treatment (**Figure A.3K-L**; methods). Points: aggregate quantification from n>14,000 fixed cells per rapalog treatment duration.

23
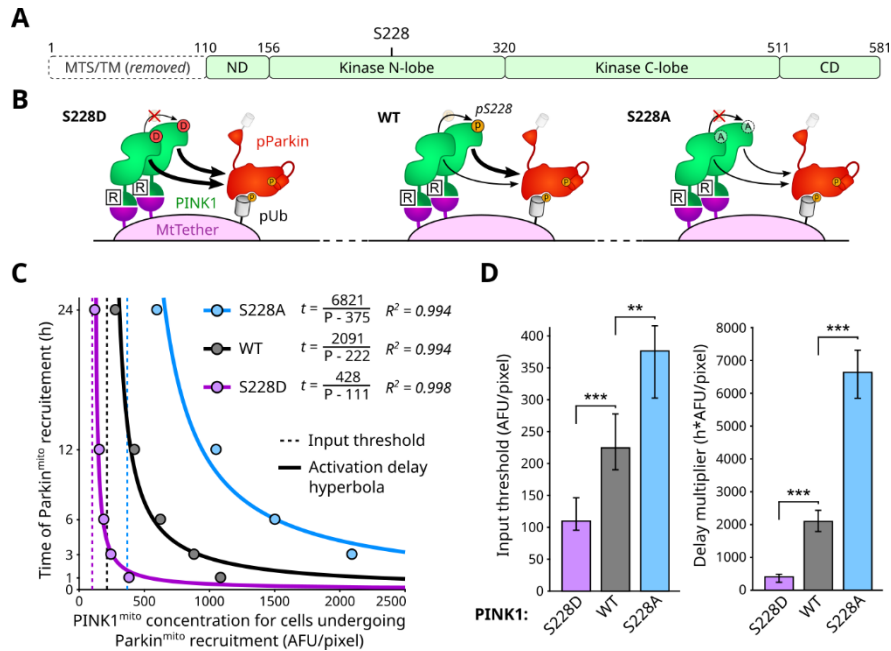
Figure 1.4: PINK1 autophosphorylation is not necessary for emergence of PINK1 input threshold or input reciprocal delay behaviors. (**A**) PINK1 domain map. MTS and transmembrane (TM) domain replaced by FKBP domain (**Figure 1.2C**). ND: N-terminal domain. CD: C-terminal domain. S228: primary functional PINK1 autophosphorylation site. (**B**) Illustration of S228 mutant consequences. S228D: phosphomimicking and non-phosphorylateable. S228A: non-phosphorylateable. (**C**) Effects of PINK1 S228 mutations on circuit behavior. Points: aggregate quantification from fixed cell measurements in **Figure A.6B**. (**D**) Statistical analysis of input threshold and delay scaler values for data in (C). Mean, 95% confidence intervals, and statistical significance calculated by bootstrap analysis (B=10,000; methods). Bonferroni multiple comparison adjustment. ** $p<0.01$; *** $p<0.001$.
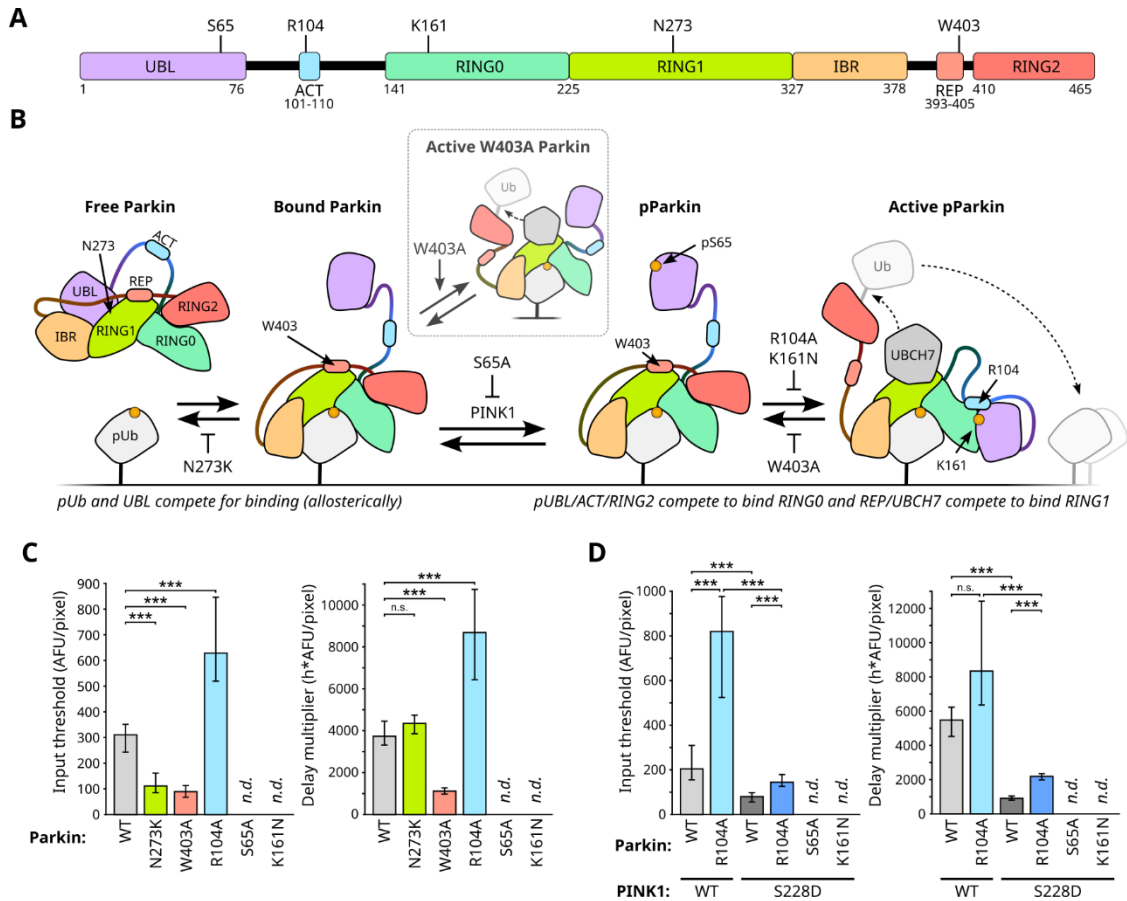
Figure 1.5: Circuit threshold and delay behaviors are differentially affected by mutations affecting Parkin activation dynamics. (A) Parkin domain map with location of mutations. UBL: ubiquitin-like. ACT: activating. REP: repressive. Four RING-like domains: RING0, RING1, IBR (in between RING), and RING2. **(B)** Effect of selected Parkin mutations on the competition-driven domain rearrangements during Parkin activation. UBCH7: an E2 Ub ligase responsible for charging Parkin[23]. Inset: unphosphorylated W403A Parkin is partially active. T-bars: repression. For effects in context of full circuit, see **Figure A.6A**. **(C)** Effect of Parkin mutations on PINK1 input threshold and reciprocal activation delay. n.d.: not determined due to lack of Parkin^{mito} recruitment. Means, 95% confidence intervals, and statistical significance calculated by bootstrap analysis (B=10,000; methods) of fixed cell populations in **Figure A.6C**. Bonferroni multiple comparison adjustment. *** p<0.001; n.s. not significant. **(D)** S228D PINK1 rescue of R104A Parkin. Representation and analysis as in (C). Single-cell data shown in **Figure A.6E**.

A

$$\frac{d(pX)}{dt} = k_{fb} * E * X * pX - k_{rev} * pX$$

Input thresh.

$$E_* = \frac{k_{rev}}{k_{fb} * X_{tot}}$$

Delay multi.

$$C_* = \frac{\ln(pX_{det} / pX_{init})}{k_{fb} * X_{tot}}$$

Input reciprocal time law

$$\text{Time from } pX_{init} \text{ to } pX_{det} = \frac{C_*}{E - E_*}$$

E

	Biological effect	Model parameter change	Predicted change from baseline		Actual change from WT Parkin	
			threshold (E_*)	delay multi. (C_*)	threshold (E_*)	delay multi. (C_*)
N273K Parkin	Parkin-pUb affinity increased	k_{rev} decreased (–)	–	no change	0.36x	1.16x (*n.s*)
W403A Parkin	Parkin activity increased (+)	k_{fb} increased (+)	–	–	0.29x	0.30x
R104A Parkin	Parkin activity decreased (–)	k_{fb} decreased (–)	+	+	2.03x	2.32x
S65A Parkin	Parkin activity decreased (– – –)	k_{fb} decreased (– – –)	+ + +	+ + +	n.d.	n.d.
K161N Parkin	Parkin activity decreased (– – –)	k_{fb} decreased (– – –)	+ + +	+ + +	n.d.	n.d.

F

Depolarized:
E accumulation

$$\frac{d(E)}{dt} = \frac{5E_*}{C_*/E_*}$$

Repolarized
E dissociation:

$$\frac{d(E)}{dt} = \frac{-50E}{C_*/E_*}$$

Figure 1.6: Input threshold and reciprocal activation delay properties arise within a minimal model of input-coupled positive feedback. **(A)** Minimal model of input-coupled positive feedback. X_{tot}: total concentration of X (note $X_{tot} = X + pX$). pX_{init}: initial concentration of pX (note $pX_{init} > 0$). pX_{det}: detection concentration of pX (note $pX_{det} \ll X_{tot}$). Parameters E_* and C_* govern input threshold and reciprocal activation delay, respectively. Derivations and model generalization described in **Appendix B**. **(B-D)** System steady state analysis (B) and relationship between input and time to reach detectable output levels (C). Black curves: algebraic solutions of (A). Points: simulated cell heterogeneity; 2000 cells were simulated, each with a randomly selected value of E and randomly selected multiplier for k_{rev}, and pX_{init}. Distributions of randomly selected values shown in (D) (methods). Colors: local point density. For analogous experimental data, see **Figure A.3I**, and **Figure 1.3C**. **(E)** The minimal model algebraically predicts experimentally observed effects of Parkin mutations on circuit's input threshold and reciprocal activation delay behavior (from **Figure 1.5C**). **(F)** The minimal model can filter out simulated transient depolarization events. Simulated depolarization (and E accumulation) for varying lengths of time, followed by repolarization (and E dissociation). Rates of E accumulation and dissociation are noted (methods). (*Figure caption continued on the next page*)

(*Figure caption continued from the previous page*) Short depolarization yields no pX (i.e., $pX = 0$). Medium depolarization yields negligible pX (i.e., $pX < pX_{det}$). Only sustained depolarization yields detectable pX (i.e., $pX \geq pX_{det}$).

1.6 Materials and methods

Cell lines and culture conditions

HeLa cells (female, RRID: CVCL_0030) were cultured with a base media consisting of RPMI (Thermo Fisher Scientific, 11875119) with 10% fetal bovine serum (Gemini Bio., #100-106) and 1x antibiotic/antimycotic (Thermo Fisher Scientific, 15240062). As with previous mitophagy studies, HeLa cells were chosen as a cell model for this study, because they lack endogenous Parkin expression[7,36]. HeLa cells were obtained from the UCSF Cell and Genome Engineering Core (CCLZR205). Cells were kept at 37C and 5% CO_2 during culturing and during live-cell microscopy.

HEK293T cells (female, RRID: CVCL_0030) were cultured for lentivirus generation with a base media consisting of DMEM (Thermo Fisher Scientific, 11965092) with 10% fetal bovine serum and 1x penicillin/streptomycin (Corning, 30-002-CI). HEK293T cells were obtained from the UCSF Cell and Genome Engineering Core (CCLZR076). Cells were cultured at 37C and 5% CO_2.

Plasmid generation

Plasmids for expressing variants of tagged Parkin: untagged Parkin (pCMV-Parkin); Untagged Parkin with E16A mutation (pCMV-Parkin(E16A)); N-terminally tagged wildtype Parkin (pCMV-mKO2-Parkin(M1)); N-terminally tagged Parkin with preserved M1L substitution (pCMV-mKO2-Parkin(M1L)), internally tagged Parkin (pCMV-Parkin-A92mKO2), and internally tagged ligase dead Parkin (pCMV-Parkin(C431N)-A92mKO2). Listed Parkin expression plasmids were derived from the pCMV-mCherry-Parkin (Addgene, #23956)[5] which

harbors an M1L substitution in Parkin. The mKO2 insert was derived from pLL3.7m-Clover-Geminin(1-110)-IRES-mKO2-Cdt(30-120) (Addgene, #83841)[63].

The backbone from pLv-EF1a-IRES-Puro (Addgene, #85132)[64] was used to create pLv-EF1a-Parkin-A92mKO2 (lentiviral stable expression vector for Parkin), pLv-EF1a-SNAP-FRB-FIS1(MTS) (lentiviral stable expression vector for MtTether-SNAP) and pLv-EF1a-FKBP-PINK1(110-581)-mNeonGreen (plasmid used for transient expression of PINK1 by lipofectamine transfection). The SNAP tag insert was derived from pSNAPf (NEB, N9183S). The FRB-Fis1 insert was derived from pC4-RhE-FRB-Fis1 (Addgene, #68056)[65]. The FKBP insert was derived from pC4M-F2E-GFP-FKBP (Addgene, #68058)[65], the PINK1(110-581) insert, lacking the 1-109 mitochondrial targeting region, was derived from pCMVTNT-PINK1-C-Myc (Addgene, #13314)[66] and the mNeonGreen insert was obtained as cDNA (Allele Biotech, ABP-FP-MNEONSB) [67]. The lentiviral doxycycline-inducible PINK1 expression vector, pLv-TetOn-FKBP-PINK1(110-581)-mNeonGreen (Neo), was created using the backbone from pLv-TetOn-MCS1-P2A-MCS2 (Neo) (Addgene, #89180).

Plasmids were assembled using standard cloning methods. Point mutations were added to expression plasmids for variants of tagged Parkin using a NEBuilder HiFi DNA Assembly Master Mix kit (NEB, E2621S). Point mutations were added to pLv-EF1a-Parkin-A92mKO2 and pLv-EF1a-FKBP-PINK1(110-581)-mNeonGreen using a Q5 site-directed mutagenesis kit (NEB, E0554S). The truncated CMV, low expression, plasmid for Parkin (pLv-CMV(trunc)-Parkin-A92mKO2) was made by 1) using the NEBuilder HiFi kit to remove the first 408 of 508 bases of the CMV enhancer/promoter region in pCMV-Parkin-A92mKO2, and 2) cloning the resulting partCMV-Parkin-mKO2 insert into the pLV-EF1a-IRES-Puro backbone. The CMV(trunc.) promoter has the sequence '*CCAAAATCAA CGGGACTTTC CAAAATGTCG TAACAACTCC*

GCCCCATTGA   CGCAAATGGG   CGGTAGGCGT   GTACGGTGGG   AGGTCTATAT

AAGCAGAGCT'. All plasmids were grown following transformation into NEB STBL competent

E. coli (NEB, C3040H). All inserts were verified via sanger sequencing (Elim

Biopharmaceuticals).

Lentiviral transduction of cell lines

Lentivirus was made for pLV-EF1a-SNAP-FRB-FIS1(MTS), pLv-EF1a-FKBP-PINK1(110-581)-mNeonGreen, pLv-EF1a-Parkin-A92mKO2, and pLv-EF1a-Parkin-A92mKO2 mutants, using HEK293T cells, pMD2.G (Addgene, 12259), pCMV-dR8.91 (NovoPro, V007548), and a lipofectamine 3000 kit (Invitrogen, L3000-015). Lentivirus was tittered for 10% transduction efficiency with 8ug/mL polybrene (EMD Millipore, TR-1003-G) in growth media.

Triple-positive (MtTether + Parkin + dox-inducible PINK1) stable cells, used in initial synthetic circuit experiments, were made by co-transducing cells with virus made from pLV-EF1a-SNAP-FRB-FIS1(MTS), pLv-EF1a-FKBP-PINK1(110-581)-mNeonGreen and pLv-EF1a-Parkin-A92mKO2. Triple positive cells were enriched as follows: TetOn-PINK1-mNG expression cassette was selected for by treatment with 400ug/mL Geniticin (Life Tech. Corp., 10131035), PINK1 expression was induced with 50ng/mL Doxycycline Hydrochloride (Sigma-Aldrich, D3072), MtTether was stained with 1:2000 SNAP-647 SiR (NEB, s9102) for 30 minutes, and positive cells were isolated with fluorescence-activated cell sorting (FACS). Following FACS, triple positive cells were allowed to expand and recover in the absence of doxycycline, to eliminate PINK1 expression prior to being frozen for storage.

Double-positive (MtTether + Parkin) HeLa cells, used for PINK1 and Parkin mutant studies, were generated in the same manner but were not transduced with the dox-inducible PINK1

expression cassette. PINK1 was instead expressed in these double-positive HeLa cells by transient transfection of pLv-EF1a-FKBP-PINK1(110-581)-mNeonGreen to allow for a greater degree of technical flexibility.

Immunofluorescence

Immunofluorescence and live-cell imaging experiments were performed in 96 well glass bottom, tissue culture treated imaging plates (Thermo Scientific Nunc, 164588). Cells were fixed in PBS (Invitrogen, AM9625) with 4% paraformaldehyde (Electron Microscopy Sciences, 15710) for 20 minutes at room temperature and were then permeabilized in PBS with 0.5% Triton X-100 (Sigma-Aldrich, 93443) for 20 minutes. Cells and then washed three times in PBS and blocked in PBS with 0.3% Triton X-100 and 3% Bovine Serum Albumin (BSA) (Fisher bioreagents, BP9703) for 1 hour. Blocked cells were then incubated in staining buffer (PBS with 0.3% Triton X-100 and 1% BSA) with primary antibody overnight at 4C and then secondary antibody for 2 hours at room temperature when applicable. Cells were stained with fluorescently conjugated primary antibodies for 2 hours at room temperature when applicable. When a primary antibody and conjugated antibody of the same host species were used, staining with the conjugated antibody was done separately from and after staining with the secondary antibody to avoid cross-reactivity. Finally, cells were stained with 1:5000 hoechst 33342 (Invitrogen, H3570) in PBS for ten minutes, and washed three times in PBS prior to imaging.

Primary antibodies: 1:500 mouse anti-Parkin (Abcam, ab77924); 1:1000 rabbit anti-phospho-Ubiquitin (CST, #70973); 1:1000 rabbit anti-Pink1 (Abcam, ab216144). Secondary antibodies: 1:1000 goat anti-mouse AF (Alexa Fluor) plus 647 (Invitrogen, A32728); 1:1000 goat anti-mouse AF 546 (Invitrogen, A11003); 1:1000 goat anti-rabbit AF plus 647 (Invitrogen,

A32728). Conjugated primary antibodies: 1:1000 rabbit anti-TOM20 AF488 (Abcam, ab205486); 1:1000 rabbit anti-TOM20 AF647 (Abcam, ab209606)

Activity assessment of Parkin tag variants

HeLa cells were grown in 96 well imaging plates. After 48 hours of growth, individual wells were each transfected with 25ng of expression plasmid for one tagged Parkin variant using a Lipofectamine 3000 kit. Media on transfected cells was replaced after 3.5 hours and cells were allowed to recover. Wells were treated with either 20uM carbonyl cyanide 3-chlorophenylhydrazone, (CCCP; Sigma Aldrich, C2759) or 2:5000 DMSO (Sigma Life Science, D2650) vehicle control for either 10 hours or 30 minutes with timing such that the treatment ended and cells were fixed 48 hours after transfection. Cells were fixed, permeabilized, subjected to immunofluorescence staining for Parkin (mouse anti-Parkin & goat anti-mouse AF647) & TOM20 (rabbit anti-TOM20 AF488), and imaged. Data was collected for three experimental replicates with two plate replicates each. This approach yielded measurements for approximately 60,000 cells per tag variant with DMSO treatment and 150,000 cells per tag variant with CCCP treatment.

Live-cell analysis of synthetic circuit

Triple- or double- positive HeLa cells were seeded in 96 well imaging plates. PINK1 expression was induced in triple-positive cells by treatment with 250ng/mL doxycycline for 48 hours. All growth, stain, wash, and imaging medias used for triple positive cells contained 250ng/mL doxycycline. PINK1 expression was induced in double-positive cells by transient transfection of 25ng/well of pLv-EF1a-FKBP-PINK1(110-581)-mNeonGreen with Lipofectamine 3000. Media on transfected cells was replaced after 3 hours and cells were allowed to recover for 48 hours.

Prior to imaging, live cells were stained with 1:1000 SNAP-AF647-SiR for 30 minutes, stained with 1:1000 Hoechst 33342 for 10 minutes, and washed twice with fresh media for 20 minutes. Hoechst staining of live HeLa cells was observed to have no effect on HeLa cell viability or growth rate. Cells were imaged in growth media once (~30 minutes) to capture the pre-treatment state. Cells were then treated with 200nM rapalog (A/C heterodimerizer, previously AP21967) (Takara Bio., 635055) and immediately subjected to live-cell microscopy with images taken every 30 minutes for 12 hours. For live-cell experiments longer than 12 hours, imaging frequency was every 45 minutes. The exact time at which each image was taken was recorded for all experiments.

Synthetic circuit modulation via USP30 inhibitor

Triple positive HeLa cells were seeded, treated with Doxycycline for 48 hours, stained, and imaged as with the live-cell imaging of the synthetic circuit described above. A 2-hour pretreatment with 1uM CMPD39 (also called USP30 inhibitor 18; MedChem Express, HY-141659) was accomplished by addition to the stain, wash, and imaging medias. Vehicle treatment for CMPD39 was 1:10,000 DMSO.

Fixed-cell analysis of synthetic circuit

Double-positive or triple-positive HeLa cells were seeded as described above. PINK1 expression was induced as described for live-cell experiments above. Individual wells of the 96 well plates were treated with rapalog for treatment durations ranging from 1 hour to 24 hours. Treatments were started at different times such that all treatments were finished at 72 hours following PINK1 expression induction. Cells were then fixed, subjected to immunofluorescence staining with rabbit anti-TOM20 AF647, and imaged.

Assessment of pUbiquitin by immunofluorescence

Double-positive HeLa cells were seeded, transfected to express Pink1, treated with rapalog for 3/6/12/24h, fixed, and permeabilized as described above. Fixed cells were stained with Hoechst and imaged to obtain initial images of Parkin and PINK1 fluorescent protein localization. Fluorescence of mKO2 and mNeonGreen was then bleached using hydrogen peroxide as described by [68]. In short, cells were incubated with a solution of 3% H_2O_2 with 20mM HCl in PBS for 2 hours with exposure to bright light. During this time, the solution was replaced after 1 hour. Complete bleaching of mKO2 and mNeonGreen was verified by imaging.

Cells were then subjected to immunofluorescence to detect phospho-Ubiquitin (pUb) and TOM20 using standard techniques as described above. Staining for pUb (rabbit anti-pUb and goat anti-rabbit AF647) was imaged in the Cy5 imaging channel to avoid any possibility of contamination by residual fluorescence from bleached fluorescent proteins. Staining for TOM20 (rabbit anti-Tom20 AF488) was imaged in the FITC channel.

Assessment of endogenous PINK1 expression levels

Parental HeLa cells and double-positive cells were seeded as above. PINK1 was expressed by transient transfection in double positive, but not in parental, cells. PINK1 transfected cells were treated with rapalog for 3/6/12/24h. Parental untransfected cells were either left untreated or were treated with 20uM CCCP for 3h. Cells were fixed and permeabilized. Fluorescence of mKO2 and mNeonGreen was then bleached as above. Cells were subjected to immunofluorescence to detect PINK1, Parkin, and Tom20. Staining for PINK1 (rabbit anti-PINK1 and goat anti-rabbit AF647) was imaged in the Cy5 imaging channel to avoid any possibility of contamination by residual fluorescence from bleached fluorescent proteins. Staining for TOM20 (rabbit anti-Tom20 AF488)

was imaged in the FITC channel. Staining for Parkin (mouse anti-Parkin & goat anti-mouse AF546) was imaged in the TRITC channel.

Microscope imaging parameters

Imaging for assessing activity of Parkin tag variants was performed on a Perkin Elmer Operetta microscope, in confocal mode, using a 20x water objective. Experiments assessing the effect of Parkin mutants on the synthetic circuit were imaged on a Perkin Elmer Phenix microscope, in confocal mode, using a 40x water objective. All other experiments were imaged on a Perkin Elmer Operetta microscope, in confocal mode, using a 40x water objective. The Phenix microscope was used during an extended period when the Operetta microscope was inoperable.

To aid in rough comparison of PINK1 input threshold values across experiments, the imaging parameters for mNeonGreen used in each experiment are listed below. Imaging conditions for fixed cell experiments was changed from 1x1 binning to 2x2 binning after initial experiments to be more comparable with live-cell experiments. Resolution has a small effect on image quantification, meaning that only rough comparison between 1x1 and 2x2 binned experiments is possible, even after accounting for exposure length and intensity binning effects. All illumination light sources were used at 100% power. Imaging parameters are listed for experiments imaged on the Phenix microscope for completeness' sake only and should not be used to compare results across microscopes.

All live-cell experiments were imaged on an Operetta microscope, with 2x2 pixel binning and a FITC exposure length of 1 second for mNeonGreen fluorescence. Initial fixed-cell circuit behavior quantification experiments as well as the G386A PINK1 mutant assessment were imaged on an Operetta microscope, with 1x1 pixel binning and a FITC exposure length of 10 seconds for

mNeonGreen fluorescence. The fixed-cell PINK1 S228 mutant assessment and pUb IF comparison experiments were imaged on an Operetta microscope, with 2x2 pixel binning and a FITC exposure length of 4 seconds for mNeonGreen fluorescence. All fixed-cell Parkin mutant assessment experiments were imaged on a Phenix microscope with 2x2 pixel binning and a FITC exposure length of 1 second for mNeonGreen fluorescence.

Western blots

Cell pellets were collected and lysed in RIPA buffer (Sigma, R0278) with Halt protease and phosphatase inhibitor cocktail (Thermo Fisher Scientific, 78440). Lysates were quantified via Bradford assay (BioRad, #5000006). Samples were run on Mini-Protean TGX 4-20% SDS-PAGE gels (Bio-Rad, 4561093). Western blotting was performed using standard approaches and according to antibody manufacturer recommendations. Odyssey blocking buffer (LI-COR Biosciences, 927-50000) diluted 1:1 with 1x TBS (Fisher scientific, BP2471-1) was used for all blocking steps and for antibody staining of S6 and pS6 blots. 3% w/v Milk (LabScientific, M0841) in 1x TBS with 1% Tween20 (Fisher scientific, BP337-500) was used for antibody staining of Parkin blots. Western blots were imaged using a LI-COR Odyssey CLx infrared imaging system. MTOR signaling assessed via levels of pS6-S235/236, a constitutive downstream target of MTOR signaling[69]. Western blot band intensities were quantified in Fiji[70]. Rapamycin, (Sigma-Aldrich, R0395). Healthy human brain lysate, whole (Novus Biologicals, NB820-59177). Primary antibodies: 1:1000 rabbit anti-pS6 (Ser235/236; Cell Signaling Technologies, 4856), 1:1000 rabbit anti-S6 (Cell Signaling Technologies, 2217), 1:1000 mouse anti-Parkin (Abcam, ab77924), 1:1000 rabbit anti-GAPDH (Cell Signaling Technologies, 5174), and 1:1000 mouse anti-GAPDH (Cell Signaling Technologies, 97166). Secondary antibodies: 1:5000 goat anti-rabbit IRDye 800CW (LI-COR, 926-32211) and 1:5000 goat anti-mouse IRDye 680LT (LI-COR, 926-68020).

Microscopy image processing and cell segmentation

All microscopy image quantification and analyses were done in MATLAB. Images were first subjected to flatfield illumination correction using pre-generated objective-specific flatfield correction estimations. Uniform background fluorescence was then removed for each image. Finally, mild fluorescence crossover from the TRITC channel (mKO2) into the FITC channel (mNeonGreen) was corrected in a pixelwise manner using a multiply and subtract compensation approach. Crossover correction was empirically calibrated for each microscope objective and for each set of exposure times used in this study. Processed images were then subjected to an in-house watershed segmentation pipeline to identify nucleus and cytoplasm boundaries for each cell. A perinuclear region was also identified by removing the outer 25% of pixels from the edge of the cytoplasm region to remove small segmentation errors due to proximity to adjacent cells.

Single-cell quantification for Parkin tag variants

For each segmented cell, foreground images were calculated for both the anti-Parkin and anti-TOM20 channels by applying a tophat filter with a radius of 8 pixels to each cell image. Co-localization of anti-Parkin and anti-TOM20 intensity was calculated as the pixelwise Pearson correlation coefficient of the foreground images for those channels. For each cell, total anti-TOM20 intensity was calculated by identifying a mitochondrial mask (anti-TOM20 foreground image intensity above 2500 AFU) and then calculating the total pixel intensity of the original anti-TOM20 image within that mask.

To compare cells with similar Parkin expression levels, a sliding window approach was used for each construct and each condition. A sliding window was used to identify cells with similar Parkin expression levels, and then the median of a score (colocalization or TOM20 staining

37

intensity) was calculated for the cells in that window. This approach estimated the given score for discrete Parkin expression levels across a range of discrete Parkin expression levels. Window center points were integer Parkin expression values ranging from 3000 to 20000 AFU/pixel. Window size was +/-850 AFU/pixel (representing 1/20 of expression range). Only cells with Parkin expression values between 3000 and 20000 AFU/pixel were used. Next, for each construct, DMSO-treated sliding median values were used to normalize the CCCP-treated sliding median values as described below. When comparing Parkin-TOM20 staining co-localization, the DMSO values at each Parkin expression level were subtracted from the corresponding CCCP-treated values at the corresponding expression level to estimate the change in localization at each Parkin expression level. When comparing total cellular anti-TOM20 staining intensity, CCCP-treated values were instead divided by the corresponding DMSO-treated values to estimate the proportion of anti-TOM20 staining remaining at each Parkin expression level. Finally, these normalized sliding medians were summarized by taking the mean value across Parkin expression levels. While all constructs were verified to have similar distributions of expression levels, this approach was used to factor out any potential Parkin expression-dependent effects which could theoretically skew the data.

Hypothesis testing was performed using a bootstrap approach. Random sampling with replacement of individual cell datapoints, followed by re-quantification of test metrics, was performed 10,000 times (B=10,000). Due to all 6 Parkin tag/mutant variants (Untagged, Internal, Nterm-M1, Nterm-M1L, LD, and Untagged-E16A) being assessed in parallel for each CCCP treatment duration, a Bonferroni multiple comparison correction was used (number of comparisons, m=5). Because the 10h and 30min CCCP treatment durations were separate experiments, they were not considered simultaneous comparisons.

Live-cell quantification for synthetic circuit

Following cell segmentation, foreground images and mitochondrial masks were calculated. Foreground images were calculated for all images by applying a 2D bandpass gaussian filter (sequential high pass gaussian with a wavelength of 50 pixels to remove background intensity and low pass gaussian with wavelength of 3 pixels to reduce pixel noise) using the filt2 MATLAB function[71]. A mitochondrial mask was calculated using the MtTether foreground image and a threshold that was calculated on a per-cell basis. This cell-specific threshold was calculated as the median pixel intensity of the original MtTether image raised to the exponent of 0.8 and multiplied by two. This approach was empirically designed to be both effective over a range of MtTether expression levels and at the pixel resolution of the live-cell images.

Next, a variety of cellular phenotypes (features) were quantified for each cell at each timepoint. Intensity co-localization features were calculated as the pixelwise Pearson correlation coefficients between pairs of foreground images. The concentration of PINK1 on mitochondria (shorthand: [PINK1^{mito}]) was estimated as the mean mNeonGreen intensity on mitochondria and was calculated as the mean pixelwise foreground intensity in the mitochondrial mask. Co-localization features and mitochondrial PINK1 features were calculated only in the perinuclear region described above to avoid intensity artifacts at cell edges. Expression level features for all channels were calculated as pixel intensity means from the original channel intensity images.

Following feature extraction, single cells were tracked from one timepoint to the next by finding the closest cell, in the next timepoint, both in distance and phenotypic similarity. This was accomplished using a distance metric defined as an empirically selected weighted sum of: the distance between nucleus centroids, the ratio of cell areas, the ratio of nucleus area, and the ratio of marker expression levels between candidate cells.

Only cells that were successfully tracked across all timepoints were used for downstream analyses. Additionally, outlier cells with high or low Parkin or MtTether expression were discarded using a threshold approach that removed approximately 5% of cells in each case. A threshold approach was also used to remove cells with high PINK1 expression levels due to masking of PINK1 recruitment to mitochondria at high expression levels. For the same reason, cells which did not show an increased co-localization between PINK1 and MtTether upon rapalog treatment were also discarded. Finally, cells with PINK1 expression levels that increased 1.5-fold or more over the course of the experiment were discarded.

Circuit inputs and responses from live-cell data

Synthetic circuit input and response estimates were quantified for each successfully tracked as follows. First, the maximum Parkin^{mito} localization was calculated as the maximum observed co-localization value between the Parkin and MtTether channels for each cell. The maximum value was used because extended Parkin^{mito} localization eventually caused mitochondrial degradation and an associated decrease in measured co-localization.

Next, the detection time of Parkin^{mito} recruitment was determined as the time at which the co-localization of Parkin and MtTether reached a value of 0.4 for each cell. The value 0.4 was chosen because it is half-way between the values measured for cells with and without Parkin^{mito} recruitment.

Finally, an estimate for the mean PINK1^{mito} concentration over time was calculated. Due to technical noise in the measurement of mean PINK1 intensity on mitochondria, data were smoothed across timepoints using a moving mean with a window size of 5 timepoints for each cell. To avoid including timepoints without PINK1^{mito} recruitment, or with intermediate, PINK1^{mito}

recruitment, smoothing did not include the pre-rapalog treatment timepoint or the timepoint immediately following rapalog treatment. The estimate for mean PINK1^{mito} concentration over time was then calculated by taking the mean value of this smoothed data from when PINK1^{mito} recruitment was first detected until either the time when Parkin^{mito} was recruited (max Parkin^{mito} localization > 0.4) or the end of the experiment (max Parkin^{mito} localization < 0.4).

Global stability over time of PINK1 targeting to mitochondria was quantified by normalizing unsmoothed single-cell traces of mean PINK1 intensity on mitochondria to the time-averaged PINK1 concentration measurement of that cell. The mean and standard deviation of the normalized cell traces were then calculated across cells for each timepoint (**Figure A.3B**).

Live-cell threshold and delay quantification

Synthetic circuit input threshold and reciprocal activation delay hyperbola were calculated from live-cell data as follows. First, a PINK1 input threshold value was calculated by: 1) taking a sliding window over the single-cell PINK1^{mito} concentration measurements (overall window width of 5% of the population size); 2) calculating the percentage of cells within each window exhibiting Parkin^{mito} recruitment (max Parkin^{mito} localization > 0.4, or, when applicable, max fraction of Parkin on mitochondria > 0.1); and 3) identifying the center point of the first window with at least 50% of cells exhibiting Parkin^{mito} recruitment. This method for calculating the PINK1 input threshold was used because it performed well with the relatively small number of datapoints obtained from live-cell experiments.

Next a hyperbolic curve was fit to the single-cell PINK1^{mito} concentration measurements and the single-cell detection times of Parkin^{mito} recruitment. This hyperbola was fit using a geometric distance, sum of squares, approach. Specifically, the "*delay multiplier*" in the following

function was optimized to obtain a fit: *Detection time of Parkin^{mito} recruitment = (delay multiplier) / ([PINK1^{mito}] – input threshold)*.

When comparing across conditions, hypothesis testing was performed using a bootstrap approach. Random sampling with replacement of individual cell datapoints, followed by re-quantification of the input threshold and delay multiplier values, was performed 10,000 times. A Bonferroni multiple comparison correction was used.

Single-cell quantification for fixed cells

Single cell quantification for fixed-cell synthetic circuit experiments was performed as follows. Following cell segmentation, foreground images were calculated as for live-cell images above. For experiments imaged with no pixel binning (initial fixed threshold experiment with WT PINK1 and WT Parkin), gaussian bandpass wavelengths used were 100 pixels and 3 pixels. A Mitochondrial mask was calculated using the anti-TOM20 mitochondrial foreground image and a fixed threshold of 1000 AFU. This approach was empirically determined to perform better for the higher resolution of un-binned images. For 2x2 binned images, (PINK1 and Parkin mutant experiments), the foreground images and mitochondrial mask were calculated exactly as described above for live-cell images. For all experiments, features were calculated the same way as described above for live-cell experiments.

Finally, single-cell data quality control was performed. Mis-segmented cells (small cell areas, small nucleus areas, or high levels of Hoechst staining in the cytoplasm) were discarded. Outlier cells with high or low Parkin expression were discarded using a threshold approach as above. Cells with low anti-TOM20 staining were discarded using a threshold approach to remove cells that had undergone mitochondrial degradation at longer timepoints. Cells with high PINK1

expression levels were discarded as above. Cells with a low co-localization of PINK1 and anti-TOM20 staining (co-localization score < 0.6) were discarded to ensure that only cells with verifiable PINK1^{mito} were analyzed.

Fixed-cell threshold and delay quantification

Synthetic circuit input threshold and reciprocal activation delay hyperbola were calculated from fixed-cell data as follows. For each rapalog treatment duration, a variant of Otsu's thresholding method was used to identify a PINK1^{mito} concentration (mean PINK1^{mito} intensity) value capable of separating the dataset into high and low Parkin^{mito} localization populations. In short, an algorithm searched for a PINK1^{mito} concentration separation value that split the dataset into high and low PINK1^{mito} concentration groups with minimized within-group size-adjusted variance for Parkin^{mito} localization. The separating value estimated the PINK1^{mito} concentration for cells undergoing Parkin^{mito} recruitment at that rapalog treatment duration, denoted here as [PINK1$^{mito\text{-}sep}$]. Within this context, the rapalog treatment duration represents time of Parkin^{mito} recruitment, allowing a hyperbolic curve to be fit to the data as with the live-cell experiments. The separating value was not calculated for conditions lacking high and low Parkin^{mito} populations.

Next a hyperbolic curve was fit to the data using a geometric distance, sum of squares, approach. Specifically, the two variables "*input threshold*" and "*delay multiplier*" in the following function were concurrently optimized to obtain a fit: *Time of Parkin^{mito} recruitment = (delay multiplier) / ([PINK1$^{mito\text{-}sep}$] – input threshold)*.

When comparing across conditions (e.g., mutants), hypothesis testing was performed using a bootstrap approach. Random sampling of individual cell datapoints with replacement, followed

by re-quantification of the input threshold and delay multiplier values, was performed 10,000 times. A Bonferroni multiple comparison correction was used.

Coloring datapoints by local point density

Local point density was calculated by counting the number of nearby points within a radius of 5% of the field of view in each direction (e.g., if the x-axis range is [0,200], then the averaging field around a point x is x ± 10).

Plotting algebraic solutions of minimal math model

The behavior of the minimal model is described by the differential equation:

$$\frac{d(pX)}{dt} = k_{fb} * E * X * pX - k_{rev} * pX$$

Properties of the minimal model are illustrated in **Figure 1.6** and **Figure A.7**. For clarity, we make use of normalized units (noted on plot axes). The total amount of X is given as $X_{tot} = X + pX$. Analysis of model properties, including sources of C_* and E_* constants, is detailed in the **Appendix B**.

In **Figure A.7B**, the forward and backward rates of the model, given by $k_{fb} * E * X * pX$ and $k_{rev} * pX$, respectively, are rewritten as $k_{rev} * X_{tot} * (E/E_*)(1 - \frac{pX}{X_{tot}})(\frac{pX}{X_{tot}})$ and $k_{rev} * X_{tot} * \frac{pX}{X_{tot}}$, respectively. The forward and backward rates are plotted for varying values of E, as multiples of E_*.

In **Figure 1.6B** and **Figure A.7C**, algebraic solutions for the *steady state* ($\frac{d(pX)}{dt} = 0$) of

$\frac{pX}{X_{tot}}$ as a function of E are plotted as $\frac{pX}{X_{tot}} = 1 - E_*/E$, and (non-physical) negative values are set

to zero.

In **Figure A.7D**, the exponential growth of pX (over time, t), from an initial value pX_{init}

to the value at which it is detected pX_{det} (**Appendix B**), is plotted. The exponential growth

function $pX = pX_{init}e^{(k_{fb}EX_{tot} - k_{off})t}$ was rewritten as $pX = pX_{init}e^{\left(\frac{E}{E_*} - 1\right)\ln\left(\frac{pX_{det}}{pX_{init}}\right)\frac{tE_*}{C_*}}$ and

plotted for varying values of E, as multiples of E_*. A value of $\frac{pX_{det}}{pX_{init}} = 100$ was used for plotting.

In **Figure 1.6C** and **Figure A.7E**, the input reciprocal time law is rewritten as

$time \ from \ pX_{init} \ to \ pX_{det} = \left(\frac{C_*}{E_*}\right)/\left(\frac{E}{E_*} - 1\right)$ and is plotted (**Figure 1.6A**; **Figure A5A**;

Appendix B). All analytical curves were plotted with MATLAB.

Heterogeneity simulation for minimal math model

Heterogenous circuit behaviors were simulated using the minimal model for input-coupled

positive feedback as follows. To simulate heterogeneity, we simulated 2000 "cells". For each

"cell", values for E, k_{rev}, and pX_{init} were sampled as follows.

E values were randomly sampled using a gamma distribution (shape parameter: 5.14; scale

parameter: 0.38). The gamma distribution was empirically fit to the observed distribution of

PINK1 input scores observed in **Figure 1.3A** using MATLAB's "fitdist" function. Noise

multiplier values for k_{rev} and for pX_{init} were randomly sampled from log normal distributions

(mu: 0; sigma: 0.5).

The detection level, pX_{det}, was set to be $pX_{det} = 100 * pX_{init}$, using the unmodified pX_{init} (pX_{init} with a noise multiplier of 1). Using these parameters, the steady state $\frac{pX}{X_{tot}}$ and time to detectable activation for each "cell" were solved analytically and plotted with MATLAB.

Transient depolarization simulation

Transient depolarization was simulated using the minimal model for input-coupled positive feedback as follows. Values for E as a function of time were calculated from the rate equations shown in **Figure 1.6F**. Rate of E association and dissociation were chosen empirically to allow a time value of 1 (in units of $\frac{C_*}{E_*}$ to be roughly interpretable as one hour. Values of pX were calculated, as a function of both *time* and value of E, using the exponential growth function described above. A value of $\frac{pX_{det}}{pX_{init}} = 100$ was used, as above.

UBL domain structure analysis

PDB accession numbers for structures shown in **Figure A.1** are as follows: hParkin, 5c1z; hUbiquitin, 1f9j; hRAD23B, 1uel; hNedd8, 1ndd; hHOIL1, 2LGY. Visualization and analysis were performed in the UCSF ChimeraX software[72]. Hydrogen bonds and salt bridges were predicted using the show hydrogen bonds option in UCSF ChimeraX.

Conservation of ubiquitin-like domains

The amino acid sequence and the metadata for 67594 annotated UBL domains in the Uniprot database were downloaded (April 4, 2019). Analysis performed with MATLAB. Entries with annotation errors were identified and discarded as follows. UBL domain entries with non-standard residues (including "J", "O", "U", "X" or "Z") or with lengths of less than 65 amino acids were discarded. Domains annotated to start at the protein's N-terminus, but which did not start

with methionine were discarded. Entries corresponding to Ubiquitin polymers rather than to UBL domains were identified as starting or ending with tandem glycines. These Ubiquitin entries were discarded to prevent over-representation in the dataset. Finally, any additional UBL domains originating from proteins containing at least one discarded domain were also discarded. This cleanup left 28447 UBL domain entries.

Alignment using traditional methods could not be used successfully due to the large number of sequences and high degree of sequence variability. Instead, the conserved positioning of specific residues in the stereotyped ubiquitin fold were used to align the sequences. Specifically, the following schema was used: hydrophobic residues in the first beta sheet at positions 1, 3 and, 5; a variable-length linker with length "x" ranging from 7 to 17 residues; hydrophobic residues in the second beta sheet at positions $5+x+1$ and $5+x+3$; hydrophobic residues in the first alpha helix at positions $5+x+9$, $5+x+12$, and $5+x+16$. These positions correspond to M1, V3, V5, V15, V17, I23, L26 and V30 of Parkin's UBL domain. Potential alignments were evaluated using scoring system where non-standard hydrophobic residues were allowed but were assigned a penalty score. Furthermore, extreme linker lengths, "x", were penalized for being too short or too long. Finally, a small tie-breaker bonus was awarded (for choosing between linker lengths) to alignments which contained a positively charged residue at the equivalent position of K27 of Parkin's UBL. This positively charged residue was used in the alignment because it was present in nearly all the published UBL domain structures which were used as reference when designing the alignment schema. Using this approach, 19623 sequences out of 28447 were successfully aligned for residues surrounding the region of interest, M1 and E16 of Parkin's UBL.

Finally, aligned sequences were separated into those belonging to N-terminal or internal UBL domains and were submitted to WebLogo3[73] to create the sequence logos used to visualize residue conservation.

Mammalian Parkin sequence alignment

Full protein sequences for mammalian Parkin were downloaded from Uniprot for human (O60260) pig (Q2L7G3), dog (A0A8C0PPD2), rat (Q9JK66), mouse (Q9WVS6), and guinea pig (H0V739). These sequences were aligned using the Clustal Omega multiple sequence alignment tool by EMBL-EBI[74].

1.7 Materials, data, and code availability

Plasmids generated in this study will be shared by Lani F. Wu upon request. Plasmids containing the mNeonGreen domain additionally require an mNeonGreen user license from Allele Biotechnologies. Single-cell microscopy quantification data has been deposited at Zenodo and are publicly available (DOI: 10.5281/zenodo.8356580). Sequence maps of plasmids generated for this study have been deposited at Zenodo and are publicly available (DOI: 10.5281/zenodo.8356580). Microscopy data reported in this paper will be shared by the Lani F. Wu upon request. All original code has been deposited at Zenodo and is publicly available (DOI: 10.5281/zenodo.8356580). Any additional information required to reanalyze the data reported in this paper is available from Lani F. Wu upon request.

1.8 References

1. Twig, G., Elorza, A., Molina, A.J.A., Mohamed, H., Wikstrom, J.D., Walzer, G., Stiles, L., Haigh, S.E., Katz, S., Las, G., et al. (2008). Fission and selective fusion govern mitochondrial segregation and elimination by autophagy. Embo J *27*, 433–446. 10.1038/sj.emboj.7601963.

2. Wang, Y., Nartiss, Y., Steipe, B., McQuibban, G.A., and Kim, P.K. (2012). ROS-induced mitochondrial depolarization initiates PARK2/PARKIN-dependent mitochondrial degradation by autophagy. Autophagy *8*, 1462–1476. 10.4161/auto.21211.

3. Yang, J.-Y., and Yang, W.Y. (2011). Spatiotemporally controlled initiation of Parkin-mediated mitophagy within single cells. Autophagy *7*, 1230–1238. 10.4161/auto.7.10.16626.

4. Zorova, L.D., Popkov, V.A., Plotnikov, E.Y., Silachev, D.N., Pevzner, I.B., Jankauskas, S.S., Babenko, V.A., Zorov, S.D., Balakireva, A.V., Juhaszova, M., et al. (2018). Mitochondrial membrane potential. Anal. Biochem. *552*, 50–59. 10.1016/j.ab.2017.07.009.

5. Narendra, D., Tanaka, A., Suen, D.-F., and Youle, R.J. (2008). Parkin is recruited selectively to impaired mitochondria and promotes their autophagy. J Cell Biology *183*, 795–803. 10.1083/jcb.200809125.

6. Narendra, D.P., Jin, S.M., Tanaka, A., Suen, D.-F., Gautier, C.A., Shen, J., Cookson, M.R., and Youle, R.J. (2010). PINK1 Is Selectively Stabilized on Impaired Mitochondria to Activate Parkin. Plos Biol *8*, e1000298. 10.1371/journal.pbio.1000298.

7. Matsuda, N., Sato, S., Shiba, K., Okatsu, K., Saisho, K., Gautier, C.A., Sou, Y., Saiki, S., Kawajiri, S., Sato, F., et al. (2010). PINK1 stabilized by mitochondrial depolarization recruits

Parkin to damaged mitochondria and activates latent Parkin for mitophagy. J Cell Biol *189*, 211–221. 10.1083/jcb.200910140.

8. Kandul, N.P., Zhang, T., Hay, B.A., and Guo, M. (2016). Selective removal of deletion-bearing mitochondrial DNA in heteroplasmic Drosophila. Nat. Commun. *7*, 13100. 10.1038/ncomms13100.

9. Suen, D.-F., Narendra, D.P., Tanaka, A., Manfredi, G., and Youle, R.J. (2010). Parkin overexpression selects against a deleterious mtDNA mutation in heteroplasmic cybrid cells. Proc. Natl. Acad. Sci. *107*, 11835–11840. 10.1073/pnas.0914569107.

10. Pickrell, A.M., and Youle, R.J. (2015). The Roles of PINK1, Parkin, and Mitochondrial Fidelity in Parkinson's Disease. Neuron *85*, 257–273. 10.1016/j.neuron.2014.12.007.

11. Ordureau, A., Sarraf, S.A., Duda, D.M., Heo, J.-M., Jedrychowski, M.P., Sviderskiy, V.O., Olszewski, J.L., Koerber, J.T., Xie, T., Beausoleil, S.A., et al. (2014). Quantitative Proteomics Reveal a Feedforward Mechanism for Mitochondrial PARKIN Translocation and Ubiquitin Chain Synthesis. Mol Cell *56*, 360–375. 10.1016/j.molcel.2014.09.007.

12. Lazarou, M., Sliter, D.A., Kane, L.A., Sarraf, S.A., Wang, C., Burman, J.L., Sideris, D.P., Fogel, A.I., and Youle, R.J. (2015). The ubiquitin kinase PINK1 recruits autophagy receptors to induce mitophagy. Nature *524*, 309–314. 10.1038/nature14893.

13. Ordureau, A., Paulo, J.A., Zhang, J., An, H., Swatek, K.N., Cannon, J.R., Wan, Q., Komander, D., and Harper, J.W. (2020). Global Landscape and Dynamics of Parkin and USP30-

Dependent Ubiquitylomes in iNeurons during Mitophagic Signaling. Mol Cell *77*, 1124-1142.e10. 10.1016/j.molcel.2019.11.013.

14. Kane, L.A., Lazarou, M., Fogel, A.I., Li, Y., Yamano, K., Sarraf, S.A., Banerjee, S., and Youle, R.J. (2014). PINK1 phosphorylates ubiquitin to activate Parkin E3 ubiquitin ligase activity. J Cell Biol *205*, 143–153. 10.1083/jcb.201402104.

15. Kazlauskaite, A., Kondapalli, C., Gourlay, R., Campbell, D.G., Ritorto, M.S., Hofmann, K., Alessi, D.R., Knebel, A., Trost, M., and Muqit, M.M.K. (2014). Parkin is activated by PINK1-dependent phosphorylation of ubiquitin at Ser65. Biochem J *460*, 127–139. 10.1042/bj20140334.

16. Koyano, F., Okatsu, K., Kosako, H., Tamura, Y., Go, E., Kimura, M., Kimura, Y., Tsuchiya, H., Yoshihara, H., Hirokawa, T., et al. (2014). Ubiquitin is phosphorylated by PINK1 to activate parkin. Nature *510*, 162–166. 10.1038/nature13392.

17. Kondapalli, C., Kazlauskaite, A., Zhang, N., Woodroof, H.I., Campbell, D.G., Gourlay, R., Burchell, L., Walden, H., Macartney, T.J., Deak, M., et al. (2012). PINK1 is activated by mitochondrial membrane potential depolarization and stimulates Parkin E3 ligase activity by phosphorylating Serine 65. Open Biol *2*, 120080. 10.1098/rsob.120080.

18. Shiba-Fukushima, K., Imai, Y., Yoshida, S., Ishihama, Y., Kanao, T., Sato, S., and Hattori, N. (2012). PINK1-mediated phosphorylation of the Parkin ubiquitin-like domain primes mitochondrial translocation of Parkin and regulates mitophagy. Sci Rep-uk *2*, 1002. 10.1038/srep01002.

19. Sauvé, V., Sung, G., Soya, N., Kozlov, G., Blaimschein, N., Miotto, L.S., Trempe, J.-F., Lukacs, G.L., and Gehring, K. (2018). Mechanism of parkin activation by phosphorylation. Nat Struct Mol Biol *25*, 623–630. 10.1038/s41594-018-0088-7.

20. Gladkova, C., Maslen, S.L., Skehel, J.M., and Komander, D. (2018). Mechanism of parkin activation by PINK1. Nature *559*, 410–414. 10.1038/s41586-018-0224-x.

21. Trempe, J.-F., Sauvé, V., Grenier, K., Seirafi, M., Tang, M.Y., Ménade, M., Al-Abdul-Wahid, S., Krett, J., Wong, K., Kozlov, G., et al. (2013). Structure of Parkin Reveals Mechanisms for Ubiquitin Ligase Activation. Science *340*, 1451–1455. 10.1126/science.1237908.

22. Tang, M.Y., Vranas, M., Krahn, A.I., Pundlik, S., Trempe, J.-F., and Fon, E.A. (2017). Structure-guided mutagenesis reveals a hierarchical mechanism of Parkin activation. Nat Commun *8*, 14697. 10.1038/ncomms14697.

23. Sauvé, V., Lilov, A., Seirafi, M., Vranas, M., Rasool, S., Kozlov, G., Sprules, T., Wang, J., Trempe, J., and Gehring, K. (2015). A Ubl/ubiquitin switch in the activation of Parkin. Embo J *34*, 2492–2505. 10.15252/embj.201592237.

24. Riley, B.E., and Olzmann, J.A. (2015). A Polyubiquitin Chain Reaction: Parkin Recruitment to Damaged Mitochondria. Plos Genet *11*, e1004952. 10.1371/journal.pgen.1004952.

25. Seirafi, M., Kozlov, G., and Gehring, K. (2015). Parkin structure and function. FEBS J. *282*, 2076–2088. 10.1111/febs.13249.

26. Bowling, J.L., Skolfield, M.C., Riley, W.A., Nolin, A.P., Wolf, L.C., and Nelson, D.E. (2019). Temporal integration of mitochondrial stress signals by the PINK1:Parkin pathway. Bmc Mol Cell Biology *20*, 33. 10.1186/s12860-019-0220-5.

27. O'Reilly, C.M., Fogarty, K.E., Drummond, R.M., Tuft, R.A., and Walsh, J.V. (2003). Quantitative Analysis of Spontaneous Mitochondrial Depolarizations. Biophys J *85*, 3350–3357. 10.1016/s0006-3495(03)74754-7.

28. Rasool, S., Soya, N., Truong, L., Croteau, N., Lukacs, G.L., and Trempe, J. (2018). PINK1 autophosphorylation is required for ubiquitin recognition. Embo Rep *19*. 10.15252/embr.201744981.

29. Rusilowicz-Jones, E.V., Jardine, J., Kallinos, A., Pinto-Fernandez, A., Guenther, F., Giurrandino, M., Barone, F.G., McCarron, K., Burke, C.J., Murad, A., et al. (2020). USP30 sets a trigger threshold for PINK1–PARKIN amplification of mitochondrial ubiquitylation. Life Sci Alliance *3*, e202000768. 10.26508/lsa.202000768.

30. Marcassa, E., Kallinos, A., Jardine, J., Rusilowicz-Jones, E.V., Martinez, A., Kuehl, S., Islinger, M., Clague, M.J., and Urbé, S. (2018). Dual role of USP30 in controlling basal pexophagy and mitophagy. Embo Rep *19*, e45595. 10.15252/embr.201745595.

31. Gersch, M., Gladkova, C., Schubert, A.F., Michel, M.A., Maslen, S., and Komander, D. (2017). Mechanism and regulation of the Lys6-selective deubiquitinase USP30. Nat Struct Mol Biol *24*, 920–930. 10.1038/nsmb.3475.

32. Harper, J.W., Ordureau, A., and Heo, J.-M. (2018). Building and decoding ubiquitin chains for mitophagy. Nat. Rev. Mol. Cell Biol. *19*, 93–108. 10.1038/nrm.2017.129.

33. Lazarou, M., Jin, S.M., Kane, L.A., and Youle, R.J. (2012). Role of PINK1 Binding to the TOM Complex and Alternate Intracellular Membranes in Recruitment and Activation of the E3 Ligase Parkin. Dev Cell *22*, 320–333. 10.1016/j.devcel.2011.12.014.

34. Belshaw, P.J., Ho, S.N., Crabtree, G.R., and Schreiber, S.L. (1996). Controlling protein association and subcellular localization with a synthetic ligand that induces heterodimerization of proteins. Proc National Acad Sci *93*, 4604–4607. 10.1073/pnas.93.10.4604.

35. Bayle, J.H., Grimley, J.S., Stankunas, K., Gestwicki, J.E., Wandless, T.J., and Crabtree, G.R. (2006). Rapamycin Analogs with Differential Binding Specificity Permit Orthogonal Control of Protein Activity. Chem Biol *13*, 99–107. 10.1016/j.chembiol.2005.10.017.

36. Denison, S.R., Wang, F., Becker, N.A., Schüle, B., Kock, N., Phillips, L.A., Klein, C., and Smith, D.I. (2003). Alterations in the common fragile site gene Parkin in ovarian and other cancers. Oncogene *22*, 8370–8378. 10.1038/sj.onc.1207072.

37. Burchell, L., Chaugule, V.K., and Walden, H. (2012). Small, N-Terminal Tags Activate Parkin E3 Ubiquitin Ligase Activity by Disrupting Its Autoinhibited Conformation. Plos One *7*, e34748. 10.1371/journal.pone.0034748.

38. Biswas, S., Roy, R., Biswas, R., and Bagchi, A. (2019). Structural analysis of the effects of mutations in Ubl domain of PARKIN leading to Parkinson's disease. Gene *726*, 144186. 10.1016/j.gene.2019.144186.

39. Han, H., Tan, J., Wang, R., Wan, H., He, Y., Yan, X., Guo, J., Gao, Q., Li, J., Shang, S., et al. (2020). PINK1 phosphorylates Drp1S616 to regulate mitophagy-independent mitochondrial dynamics. EMBO Rep. *21*, e48686. 10.15252/embr.201948686.

40. Pryde, K.R., Smith, H.L., Chau, K.-Y., and Schapira, A.H.V. (2016). PINK1 disables the anti-fission machinery to segregate damaged mitochondria for mitophagy. J. Cell Biol. *213*, 163–171. 10.1083/jcb.201509003.

41. Okatsu, K., Oka, T., Iguchi, M., Imamura, K., Kosako, H., Tani, N., Kimura, M., Go, E., Koyano, F., Funayama, M., et al. (2012). PINK1 autophosphorylation upon membrane potential dissipation is essential for Parkin recruitment to damaged mitochondria. Nat. Commun. *3*, 1016. 10.1038/ncomms2016.

42. Aerts, L., Craessaerts, K., Strooper, B.D., and Morais, V.A. (2015). PINK1 Kinase Catalytic Activity Is Regulated by Phosphorylation on Serines 228 and 402*. J Biol Chem *290*, 2798–2811. 10.1074/jbc.m114.620906.

43. Yi, W., MacDougall, E.J., Tang, M.Y., Krahn, A.I., Gan-Or, Z., Trempe, J.-F., and Fon, E.A. (2019). The landscape of Parkin variants reveals pathogenic mechanisms and therapeutic targets in Parkinson's disease. Hum. Mol. Genet. *28*, 2811–2825. 10.1093/hmg/ddz080.

44. Stevens, M.U., Croteau, N., Eldeeb, M.A., Antico, O., Zeng, Z.W., Toth, R., Durcan, T.M., Springer, W., Fon, E.A., Muqit, M.M., et al. (2023). Structure-based design and characterization of Parkin-activating mutations. Life Sci. Alliance *6*, e202201419. 10.26508/lsa.202201419.

45. Sauvé, V., Sung, G., MacDougall, E.J., Kozlov, G., Saran, A., Fakih, R., Fon, E.A., and Gehring, K. (2022). Structural basis for feedforward control in the PINK1/Parkin pathway. EMBO J. *41*, e109460. 10.15252/embj.2021109460.

46. Xiao, B., Goh, J.-Y., Xiao, L., Xian, H., Lim, K.-L., and Liou, Y.-C. (2017). Reactive oxygen species trigger Parkin/PINK1 pathway–dependent mitophagy by inducing mitochondrial recruitment of Parkin. J Biol Chem *292*, 16697–16708. 10.1074/jbc.m117.787739.

47. Xiao, B., Deng, X., Lim, G.G.Y., Xie, S., Zhou, Z.D., Lim, K.-L., and Tan, E.-K. (2017). Superoxide drives progression of Parkin/PINK1-dependent mitophagy following translocation of Parkin to mitochondria. Cell Death Dis *8*, e3097–e3097. 10.1038/cddis.2017.463.

48. Hung, C.-M., Lombardo, P.S., Malik, N., Brun, S.N., Hellberg, K., Nostrand, J.L.V., Garcia, D., Baumgart, J., Diffenderfer, K., Asara, J.M., et al. (2021). AMPK/ULK1-mediated phosphorylation of Parkin ACT domain mediates an early step in mitophagy. Sci Adv *7*, eabg4544. 10.1126/sciadv.abg4544.

49. Rasool, S., Veyron, S., Soya, N., Eldeeb, M.A., Lukacs, G.L., Fon, E.A., and Trempe, J.-F. (2022). Mechanism of PINK1 activation by autophosphorylation and insights into assembly on the TOM complex. Mol Cell *82*, 44-59.e6. 10.1016/j.molcel.2021.11.012.

50. Okatsu, K., Uno, M., Koyano, F., Go, E., Kimura, M., Oka, T., Tanaka, K., and Matsuda, N. (2013). A Dimeric PINK1-containing Complex on Depolarized Mitochondria Stimulates Parkin Recruitment*. J. Biol. Chem. *288*, 36372–36384. 10.1074/jbc.m113.509653.

51. Haywood, A.F., and Staveley, B.E. (2004). parkin counteracts symptoms in a Drosophila model of Parkinson's disease. BMC Neurosci. *5*, 14. 10.1186/1471-2202-5-14.

52. Rusilowicz-Jones, E.V., Barone, F.G., Lopes, F.M., Stephen, E., Mortiboys, H., Urbé, S., and Clague, M.J. (2022). Benchmarking a highly selective USP30 inhibitor for enhancement of mitophagy and pexophagy. Life Sci Alliance *5*, e202101287. 10.26508/lsa.202101287.

53. Liang, J., Martinez, A., Lane, J.D., Mayor, U., Clague, M.J., and Urbé, S. (2015). USP30 deubiquitylates mitochondrial Parkin substrates and restricts apoptotic cell death. Embo Rep *16*, 618–627. 10.15252/embr.201439820.

54. Cunningham, C.N., Baughman, J.M., Phu, L., Tea, J.S., Yu, C., Coons, M., Kirkpatrick, D.S., Bingol, B., and Corn, J.E. (2015). USP30 and parkin homeostatically regulate atypical ubiquitin chains on mitochondria. Nat Cell Biol *17*, 160–169. 10.1038/ncb3097.

55. Bingol, B., Tea, J.S., Phu, L., Reichelt, M., Bakalarski, C.E., Song, Q., Foreman, O., Kirkpatrick, D.S., and Sheng, M. (2014). The mitochondrial deubiquitinase USP30 opposes parkin-mediated mitophagy. Nature *510*, 370–375. 10.1038/nature13418.

56. Cornelissen, T., Haddad, D., Wauters, F., Humbeeck, C.V., Mandemakers, W., Koentjoro, B., Sue, C., Gevaert, K., Strooper, B.D., Verstreken, P., et al. (2014). The deubiquitinase USP15 antagonizes Parkin-mediated mitochondrial ubiquitination and mitophagy. Hum Mol Genet *23*, 5227–5242. 10.1093/hmg/ddu244.

57. Wang, L., Cho, Y.-L., Tang, Y., Wang, J., Park, J.-E., Wu, Y., Wang, C., Tong, Y., Chawla, R., Zhang, J., et al. (2018). PTEN-L is a novel protein phosphatase for ubiquitin

dephosphorylation to inhibit PINK1–Parkin-mediated mitophagy. Cell Res *28*, 787–802. 10.1038/s41422-018-0056-0.

58. Burman, J.L., Pickles, S., Wang, C., Sekine, S., Vargas, J.N.S., Zhang, Z., Youle, A.M., Nezich, C.L., Wu, X., Hammer, J.A., et al. (2017). Mitochondrial fission facilitates the selective mitophagy of protein aggregates. J. Cell Biol. *216*, 3231–3247. 10.1083/jcb.201612106.

59. Jilkine, A., Angenent, S.B., Wu, L.F., and Altschuler, S.J. (2011). A Density-Dependent Switch Drives Stochastic Clustering and Polarization of Signaling Molecules. Plos Comput Biol *7*, e1002271. 10.1371/journal.pcbi.1002271.

60. Chen, Y., and Ferrell, J.E. (2021). C. elegans colony formation as a condensation phenomenon. Nat Commun *12*, 4947. 10.1038/s41467-021-25244-9.

61. Kiyatkin, A., Aksamitiene, E., Markevich, N.I., Borisov, N.M., Hoek, J.B., and Kholodenko, B.N. (2006). Scaffolding Protein Grb2-associated Binder 1 Sustains Epidermal Growth Factor-induced Mitogenic and Survival Signaling by Multiple Positive Feedback Loops*. J Biol Chem *281*, 19925–19938. 10.1074/jbc.m600482200.

62. Borisov, N., Aksamitiene, E., Kiyatkin, A., Legewie, S., Berkhout, J., Maiwald, T., Kaimachnikov, N.P., Timmer, J., Hoek, J.B., and Kholodenko, B.N. (2009). Systems-level interactions between insulin–EGF networks amplify mitogenic signaling. Mol Syst Biol *5*, 256–256. 10.1038/msb.2009.19.

63. Bajar, B.T., Lam, A.J., Badiee, R.K., Oh, Y.-H., Chu, J., Zhou, X.X., Kim, N., Kim, B.B., Chung, M., Yablonovitch, A.L., et al. (2016). Fluorescent indicators for simultaneous reporting of all four cell cycle phases. Nat. Methods *13*, 993–996. 10.1038/nmeth.4045.

64. Hayer, A., Shao, L., Chung, M., Joubert, L.-M., Yang, H.W., Tsai, F.-C., Bisaria, A., Betzig, E., and Meyer, T. (2016). Engulfed cadherin fingers are polarized junctional structures between collectively migrating endothelial cells. Nat. Cell Biol. *18*, 1311–1323. 10.1038/ncb3438.

65. Narendra, D., Kane, L.A., Hauser, D.N., Fearnley, I.M., and Youle, R.J. (2010). p62/SQSTM1 is required for Parkin-induced mitochondrial clustering but not mitophagy; VDAC1 is dispensable for both. Autophagy *6*, 1090–1106. 10.4161/auto.6.8.13426.

66. Beilina, A., Brug, M.V.D., Ahmad, R., Kesavapany, S., Miller, D.W., Petsko, G.A., and Cookson, M.R. (2005). Mutations in PTEN-induced putative kinase 1 associated with recessive parkinsonism have differential effects on protein stability. Proc. Natl. Acad. Sci. *102*, 5703–5708. 10.1073/pnas.0500617102.

67. Shaner, N.C., Lambert, G.G., Chammas, A., Ni, Y., Cranfill, P.J., Baird, M.A., Sell, B.R., Allen, J.R., Day, R.N., Israelsson, M., et al. (2013). A bright monomeric green fluorescent protein derived from Branchiostoma lanceolatum. Nat. Methods *10*, 407–409. 10.1038/nmeth.2413.

68. Lin, J., Fallahi-Sichani, M., Chen, J., and Sorger, P.K. (2016). Cyclic Immunofluorescence (CycIF), A Highly Multiplexed Method for Single-cell Imaging. Curr Protoc Chem Biology *8*, 251–264. 10.1002/cpch.14.

69. Chung, J., Kuo, C.J., Crabtree, G.R., and Blenis, J. (1992). Rapamycin-FKBP specifically blocks growth-dependent activation of and signaling by the 70 kd S6 protein kinases. Cell *69*, 1227–1236. 10.1016/0092-8674(92)90643-q.

70. Schindelin, J., Arganda-Carreras, I., Frise, E., Kaynig, V., Longair, M., Pietzsch, T., Preibisch, S., Rueden, C., Saalfeld, S., Schmid, B., et al. (2012). Fiji: an open-source platform for biological-image analysis. Nat. Methods *9*, 676–682. 10.1038/nmeth.2019.

71. Greene, C. (2017). Filt2 2D geospatial data filter (MATLAB Central File Exchange).

72. Pettersen, E.F., Goddard, T.D., Huang, C.C., Meng, E.C., Couch, G.S., Croll, T.I., Morris, J.H., and Ferrin, T.E. (2021). UCSF ChimeraX: Structure visualization for researchers, educators, and developers. Protein Sci. *30*, 70–82. 10.1002/pro.3943.

73. Crooks, G.E., Hon, G., Chandonia, J.-M., and Brenner, S.E. (2004). WebLogo: A Sequence Logo Generator. Genome Res. *14*, 1188–1190. 10.1101/gr.849004.

74. Madeira, F., Pearce, M., Tivey, A.R.N., Basutkar, P., Lee, J., Edbali, O., Madhusoodanan, N., Kolesnikov, A., and Lopez, R. (2022). Search and sequence analysis tools services from EMBL-EBI in 2022. Nucleic Acids Res. *50*, W276–W279. 10.1093/nar/gkac240.

APPENDIX A
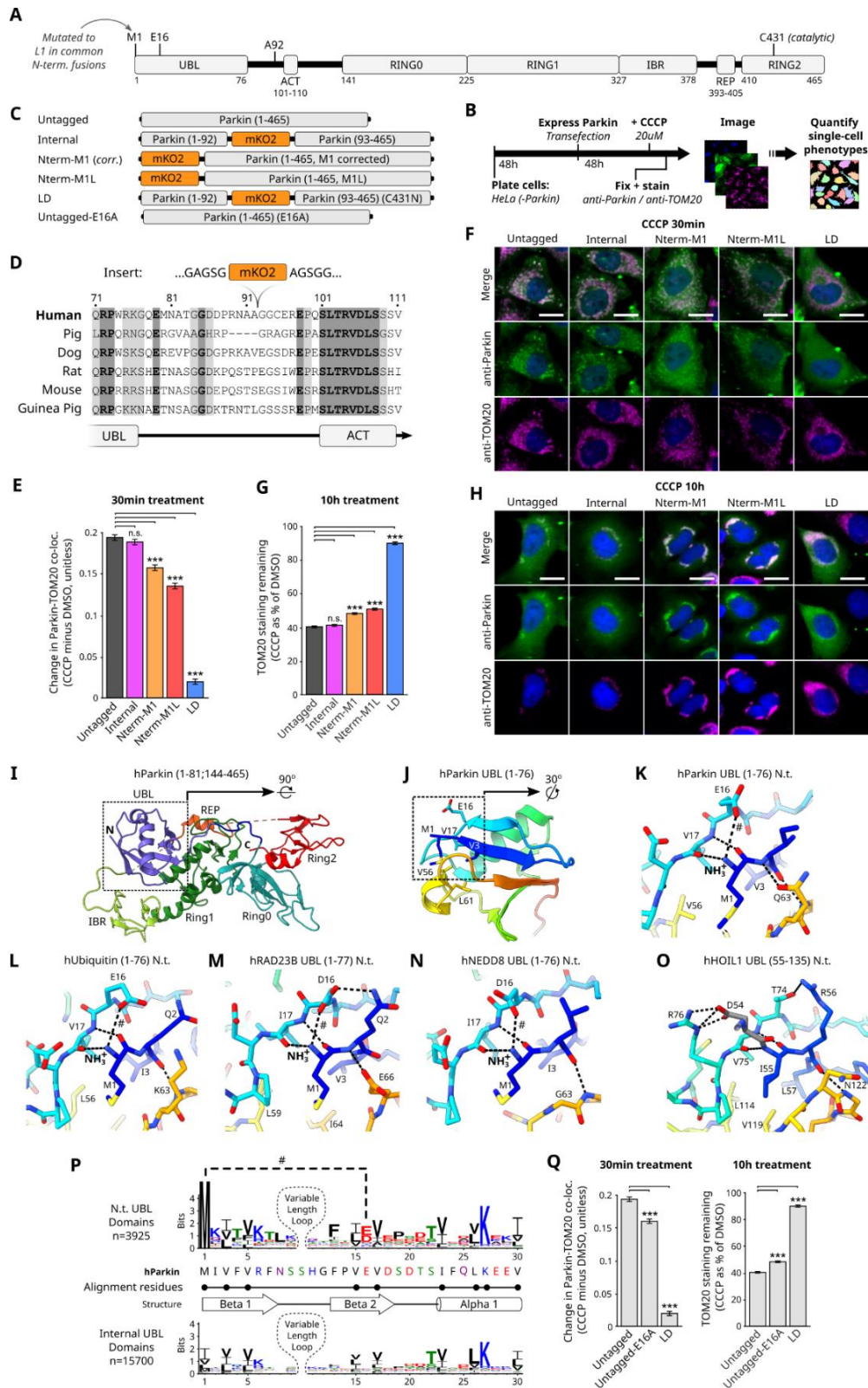
Supplementary figures

Figure A.1: Identification of an internal Parkin tagging site that preserves function. (A) Parkin domain map. UBL: ubiquitin-like. ACT: activating. REP: repressive. Four RING-like domains: RING0, RING1, IBR (in between RING), (*Figure caption continued on the next page*)

(*Figure caption continued from the previous page*) and RING2. Selected residues marked. M1 indicates Parkin's N-terminal methionine. **(B)** Immunofluorescence (IF) approach for assessing Parkin function. HeLa cells lack endogenous Parkin expression. Parkin expressed by transient transfection (methods). Anti-TOM20 stains mitochondria. Bar length not to scale. **(C)** Parkin fusion proteins, assessed for activity. M1L mutation was carried over from the mCherry-Parkin cloning source and was corrected to make Nterm-M1(corr.). LD: ligase dead **(D)** Conservation of residues at Parkin's internal tagging site. **(E)** Change in Parkin localization due to CCCP treatment (methods). Single cell data: **Figure A.2.A-B**. Co-localization (Co-loc.), foreground intensity correlation (Pearson; methods). Mean, 95% confidence intervals, and statistical significance calculated by bootstrap analysis (B=10,000). Bonferroni multiple comparison adjustment. ***p<0.001; n.s.: not significant. **(F)** Representative images showing Parkin recruitment. Scale bars: 20um. **(G)** Mean TOM20 depletion due to CCCP treatment. Single cell data: **Figure A.2.C-D**. Bootstrap approach as in (E). AFU, arbitrary fluorescence units. **(H)** Representative images showing TOM20 loss. Scale bars: 20um. **(I-K)** Human Parkin structure (PDB: 5C1Z). **(I)** Full protein. **(J)** UBL domain. **(K)** N-terminus (N.t.) of UBL domain. Carbon: color gradient. Oxygen: red. Nitrogen: blue. Sulfur, yellow. Dotted lines: predicted interactions. #: predicted salt bridge between E16 and the N.t. NH_3^+ which would be disrupted by any N-terminal tag. **(L-N)** N.t. structures of human Ubiquitin and other N.t. UBL domains (PDB: 1F9J, 1UEL, and 1NDD respectively). **(O)** N.t. structure of human HOIL1's internal UBL domain (PDB: 2LGY). N.t. of ubiquitin fold stabilized by additional interactions involving D54. Gray coloring: N-terminal extension to canonical UBL fold. **(P)** Sequence logo showing amino acid conservation in UBL domains. Analysis across unique UBL domains in the Uniprot database (methods). Residues used for motif-based alignment are marked (methods). **(Q)** E16A Parkin mutant phenocopies functional defect of N-terminal tags. Functional evaluation as in (E-G).
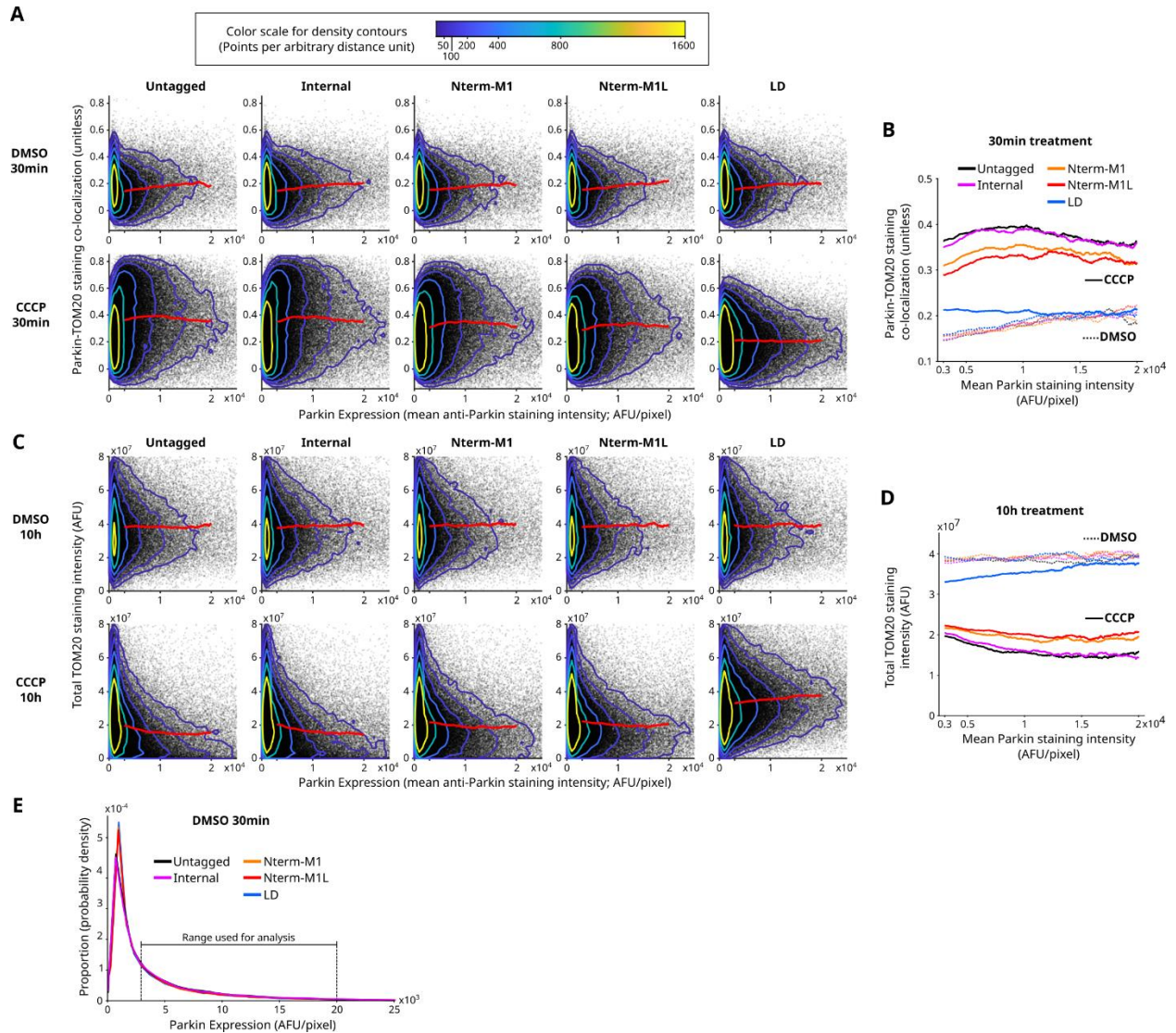
Figure A.2: Raw data for comparison of Parkin tagging strategies. (A-B) Parkin recruitment to mitochondria (TOM20): Single-cell data (A) and single cell data analysis approach (B) used to generate **Figure A.1E**. **(A)** Single cell Parkin recruitment to mitochondria (TOM20) versus Parkin expression. Points, single cells; contours, datapoint density; red lines, sliding medians. Single-cell data from three experimental replicates was pooled. DMSO: n=~60,000 cells/condition; CCCP: n=~150,000 cells/condition; ~35% of cells had Parkin expression within the range used to calculate the moving medians, 3000-20000 AFU/px. **(B)** Parkin recruitment to mitochondria (TOM20) as a function of Parkin expression. Data are sliding medians of single-cell data shown in (A). AFU, arbitrary fluorescence units. **(C-D)** Mitochondrial (TOM20) loss: single cell data (C) and single cell data analysis approach (D) used to generate **Figure A.1G**. Depiction and analysis as for (A-B) respectively. **(E)** Parkin fusions were expressed at similar levels. Distribution of single cell Parkin expression levels for each Parkin fusion. Parkin expression level was measured as the mean anti-Parkin staining intensity in images. Range used to make moving medians in (A-D) is noted.
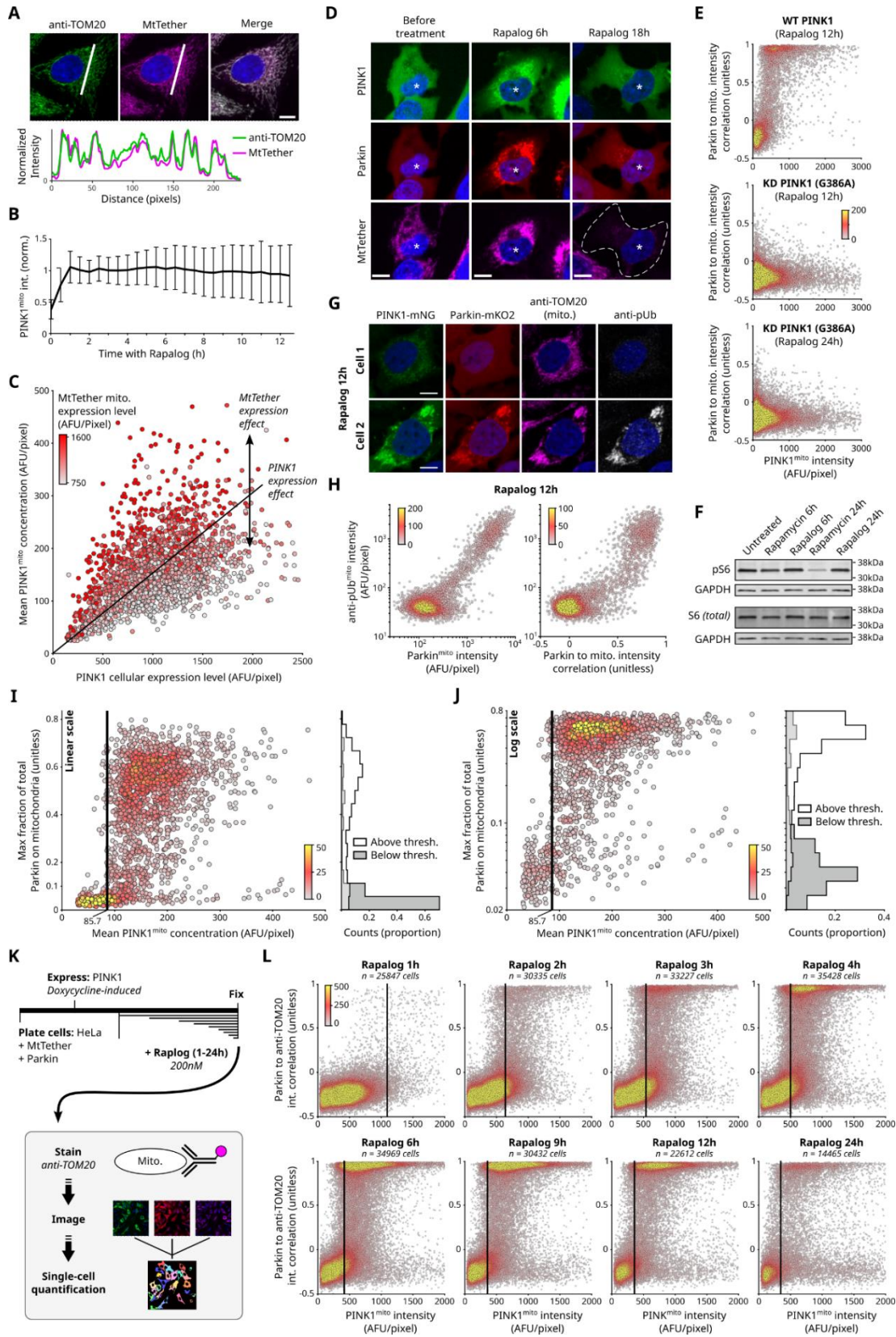
(*Figure caption on the next page*)

(*Figure caption continued from the previous page*) **Figure A.3: Characterization of the PINK1/Parkin synthetic circuit. (A)** MtTether localization matches that of mitochondrial protein TOM20. Top: Representative images. Bottom: pixel intensities along white lines in images. Scale bar: 20um. **(B)** Average PINK1^{mito} levels are relatively stable over time. Mean and standard deviation, per imaging timepoint, across 1987 normalized cell traces (methods). **(C)** Relationship between PINK1^{mito} and cellular expression of PINK1 and MtTether. Points: 1987 individual cells, colored by MtTether expression level. Lines: empirical trends **(D)** Representative live-cell imaging of mitochondrial loss following prolonged rapalog-driven PINK1^{mito} and Parkin^{mito} recruitment. Asterisk: cell of interest. Dotted line: cell boundary. Scale bars: 10um. **(E)** Kinase dead (KD) PINK1 (G386A) is not capable of recruiting Parkin. Points: single-cell measurements of fixed cells, colored by local point density. **(F)** Effect of rapalog treatment on mTOR signaling (pS6; methods). Rapamycin: positive control, 100nM. Rapalog: 200nM. **(G-H)** Parkin^{mito} recruitment correlated with pUb^{mito} levels. **(G)** Representative images of two cells: with or without anti-pUb^{mito} staining and Parkin^{mito} fluorescence. Scale bars: 10um. **(H)** Fixed cell analysis and comparison of anti-pUb staining. Left: linear correlation between amounts of pUb^{mito} and Parkin^{mito}. Right: Parkin^{mito} intensity correlation detects Parkin^{mito} recruitment before pUb^{mito} levels detectably rise. Points: single-cell measurements of fixed cells, colored by local point density. **(I-J)** Re-analysis of circuit input and response from **Figure 1.3A** for alternative response metric: max fraction of Parkin on mitochondria. Vertical line, re-calculated PINK1 input threshold (methods). Points, 1987 individual cells, colored by local point density. Y-axis shown with linear (I) and log (J) scales for clearer visualization. **(K-L)** Measurement of the PINK1/Parkin synthetic circuit behavior using fixed cell analysis. **(K)** Experimental approach. Bar length not to scale. **(L)** Single-cell Parkin^{mito} localization versus PINK1^{mito} concentration at various rapalog treatment durations. Points: single-cell measurements of fixed cells, colored by local point density, pooled from three experimental replicates. Vertical lines, PINK^{mito} concentration for cells undergoing Parkin^{mito} recruitment (methods). Progressive datapoint scarcity caused by mitochondrial degradation.
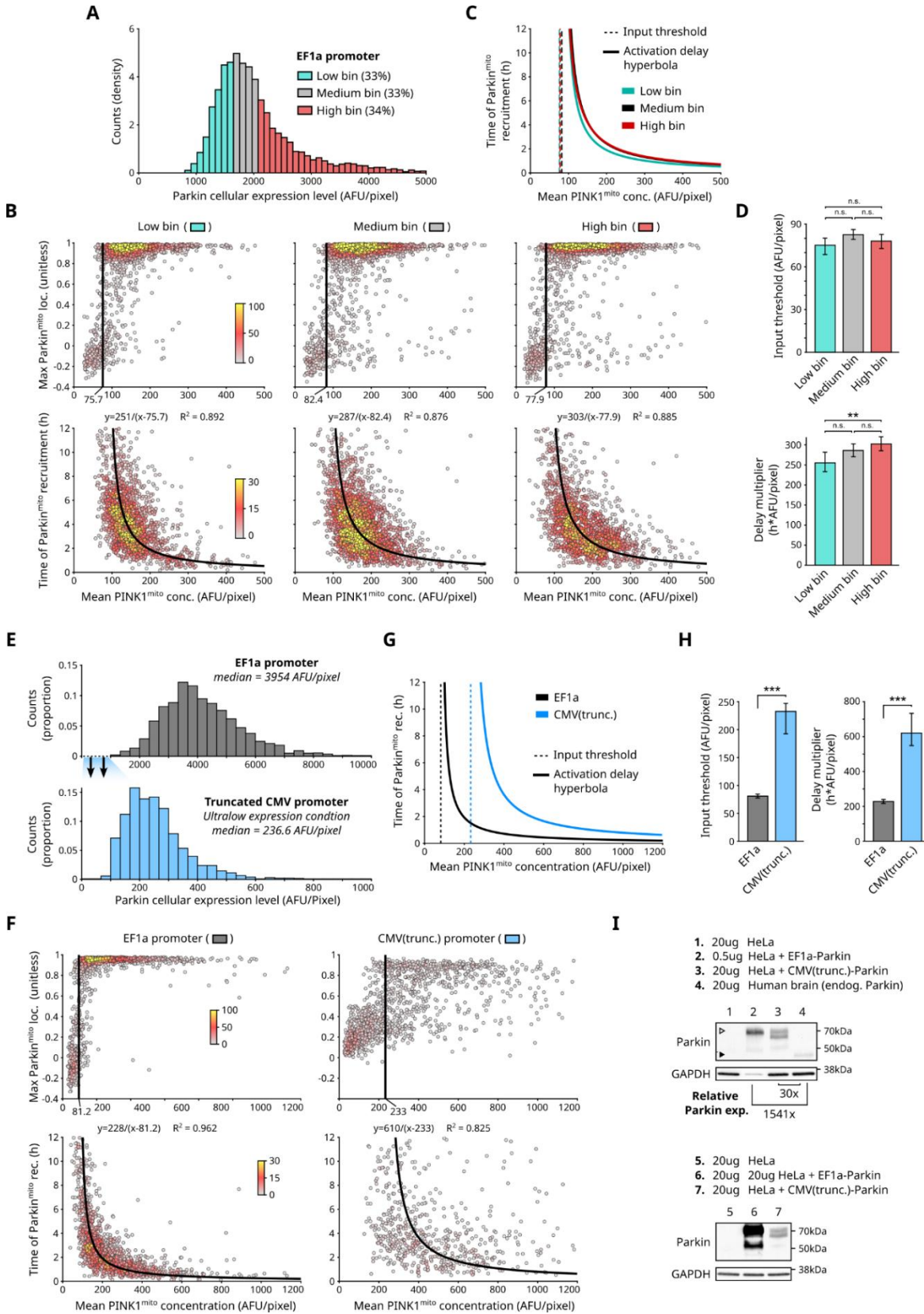
(*Figure caption on the next page*)

(*Figure caption continued from the previous page*) **Figure A.4: Effect of Parkin expression on PINK1/Parkin synthetic circuit dynamics. (A-D)** The effect of Parkin expression levels on synthetic circuit behavior. **(A)** Distribution of single-cell Parkin expression levels, from the synthetic circuit's standard EF1a promoter, split into three equally sized groups (percentage of total noted). Live-cell data from four experiments was pooled. Counts normalized to bin width (density). **(B)** Quantification of PINK1 input threshold (top) and reciprocal activation delay hyperbola (bottom) for cells in expression groups in (A). Points: individual cells, colored by local point density. **(C)** Threshold and hyperbolas from (B), overlaid. **(D)** Bootstrap statistical analysis of input threshold and delay scaler values for data in (B-C). Mean, 95% confidence intervals, and statistical significance calculated by bootstrap analysis (B=10,000). Bonferroni multiple comparison adjustment. **p<0.01; n.s.: not significant. **(E-H)** Circuit behaviors preserved at ultralow Parkin expression levels. **(E)** Ultralow Parkin expression driven by a truncated CMV promoter, CMV(trunc.), compared to that of the EF1a promoter, measured by fluorescence microscopy. Values for EF1a promoter differ from (A) due to longer exposure times required to image CMV(trunc.) condition. **(F)** Quantification of circuit behaviors for expression conditions in (E) from live cells. Increased noise in the CMV(trunc.) from Parkin expression approaching instrument's background fluorescence levels. **(G)** Threshold and hyperbolas from (F), overlaid. **(H)** Bootstrap statistical analysis of input threshold and delay scaler values for data in (F-G). Mean, 95% confidence intervals, and statistical significance calculated by bootstrap analysis (B=10,000). Bonferroni multiple comparison adjustment. ***p<0.001. **(I)** Characterization of Parkin expression levels compared to that of endogenous Parkin in human brain lysate. Amount of loaded protein is listed for each lane. Filled/empty triangles indicate endogenous/mKO2-tagged Parkin respectively. Band intensity quantification shown for lane 2 and 3 normalized to GAPDH and compared to lane 4 (methods). Fold difference of expression between EF1a and CMV(trunc.) differs from (E) due to effect of background fluorescence in CMV(trunc.) condition. Double band in lane 3 may indicate presence of truncated protein. Decreased protein function due to truncation may contribute to increased threshold and delay in (F-H) causing overestimation of the repressive effect of ultralow Parkin expression.
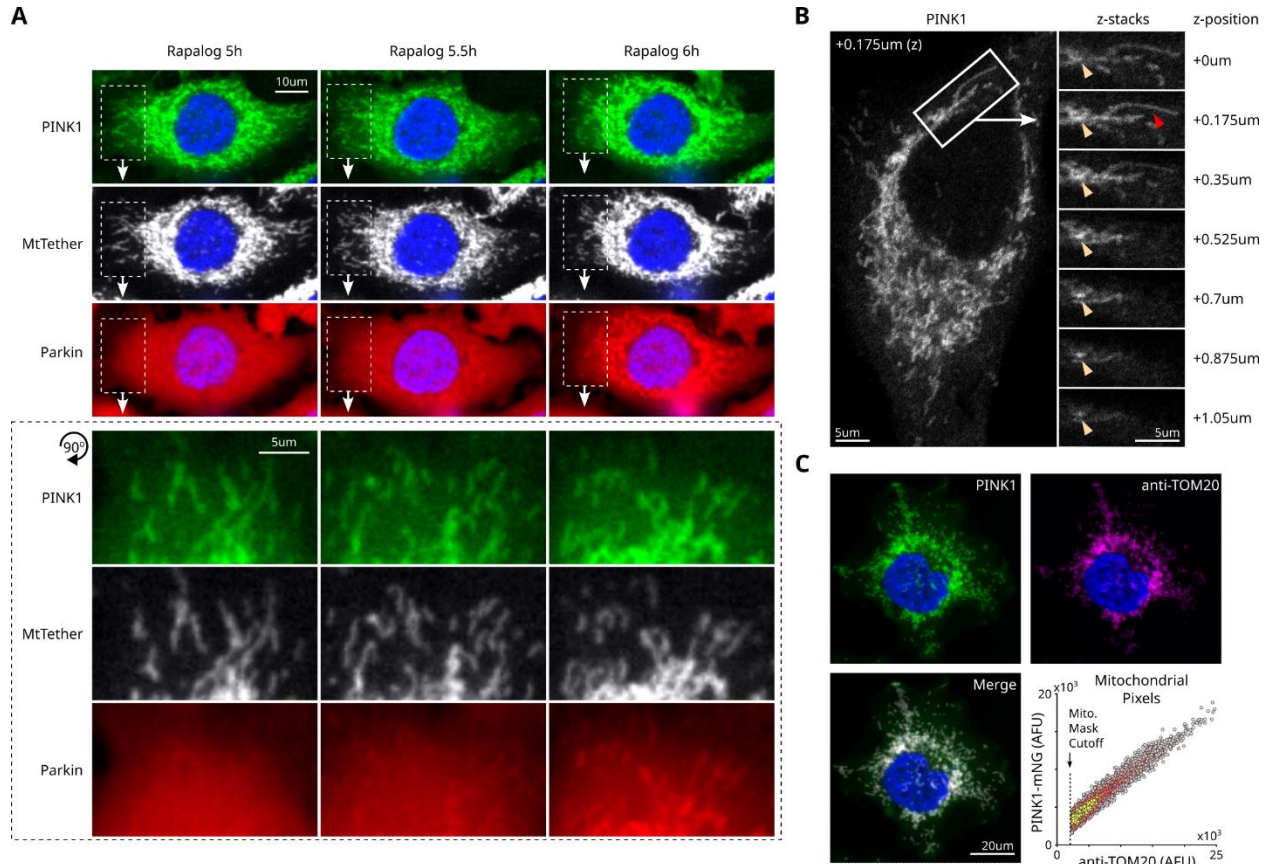
Figure A.5: Parkin and PINK1 are uniformly recruited to mitochondria. (A) Peripheral, isolated mitochondria recruit Parkin at similar time as the rest of the mitochondrial network. Timelapse images of a representative cell undergoing Parkin recruitment. Top: full cell. Bottom: Magnified view of cell periphery, rotated. Scale bar sizes marked. **(B)** Imaging z-stack of mitochondrial PINK1, 3h rapalog treatment. Red arrow, uniform PINK1 recruitment along a mitochondrion. Yellow arrows, region with higher intensity associated with overlapping mitochondria or mitochondrial structures extending vertically through z-stacks. **(C)** PINK1 distribution on mitochondria compared that of TOM20. Representative cell, 1h rapalog treatment. Graph, pixel intensity correlation. Points, pixels on mitochondria mask (methods), colored by local point density. PINK1 distribution on mitochondrial membrane is as uniform as that of TOM20 at this measurement precision.
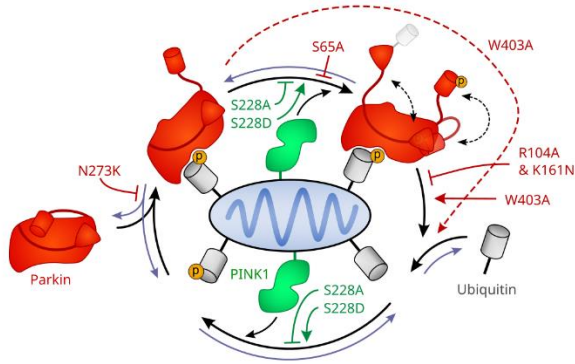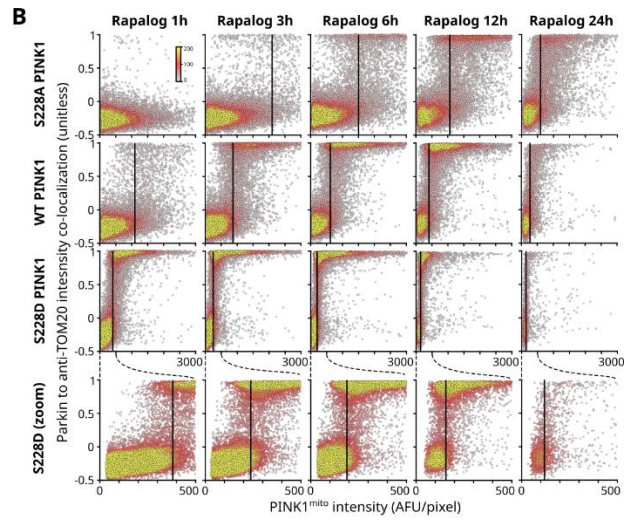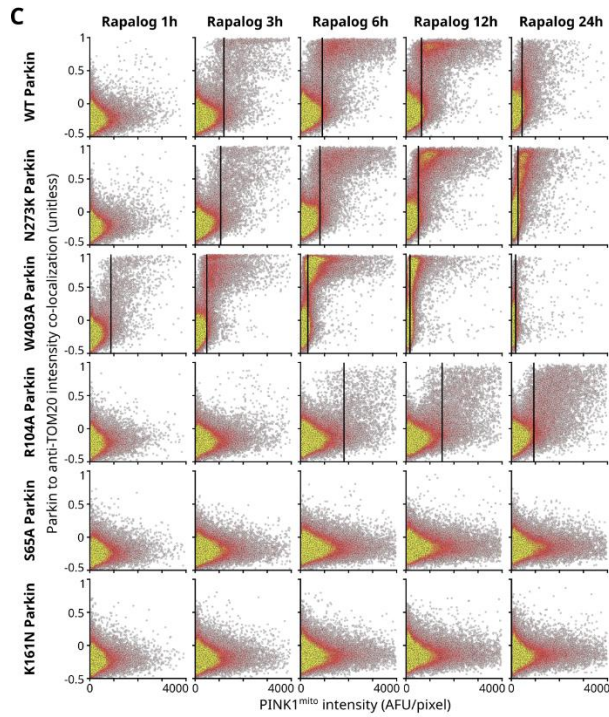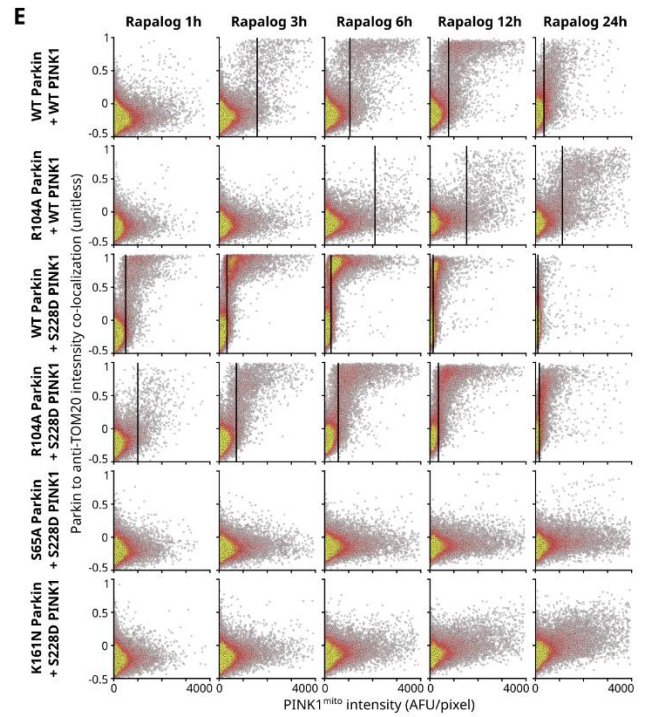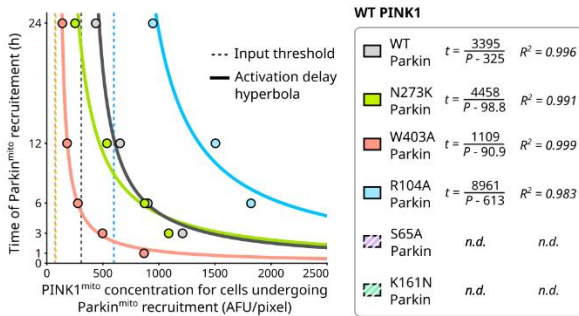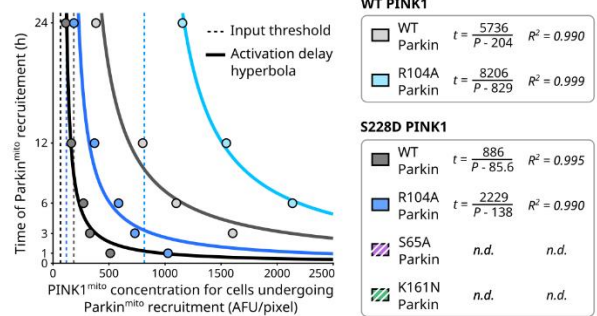
(*Figure caption on the next page*)

(*Figure caption continued from the previous page*) **Figure A.6: Single-cell data for evaluating behavior of PINK1 and Parkin mutants. (A)** PINK1 (green) and Parkin (red) mutation effects in full circuit context. Mutation arrows/T-bars: enhancement/repression (resp.). All affects are modulatory, except for S65A which completely blocks Parkin phosphorylation by PINK1. Relative strength of W403A bypass is unknown. **(B)** Single-cell source data for **Figure 1.4C-D**. Points: single-cell measurements of fixed cells, colored by local point density. Single-cell data pooled from two plate replicates. Vertical black lines: estimated $PINK1^{mito}$ concentration of cells undergoing $Parkin^{mito}$ recruitment (methods). Progressive datapoint scarcity caused by mitochondrial degradation. Bottom row: rescaled x-axis for clearer visualization. **(C)** Single-cell source data for **Figure 1.5C**. Representation and analysis as in (B). Single-cell data pooled from two experimental replicates of three plate replicates each. **(D)** Effect of Parkin mutations on PINK1 circuit behavior. Points: aggregate quantification from fixed cell measurements in (C). n.d.: not determined due to lack of $Parkin^{mito}$ recruitment. **(E-F)** Single-cell source data for **Figure 1.5D**. Representation and analysis as in (C-D). Single-cell data pooled from two experimental replicates of three plate replicates each.

A
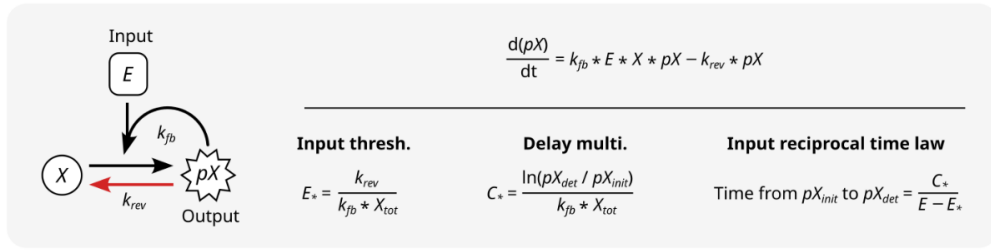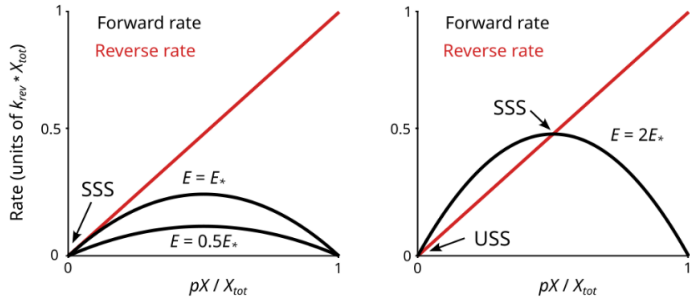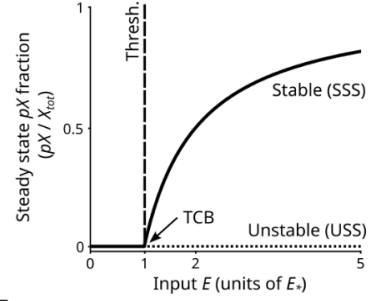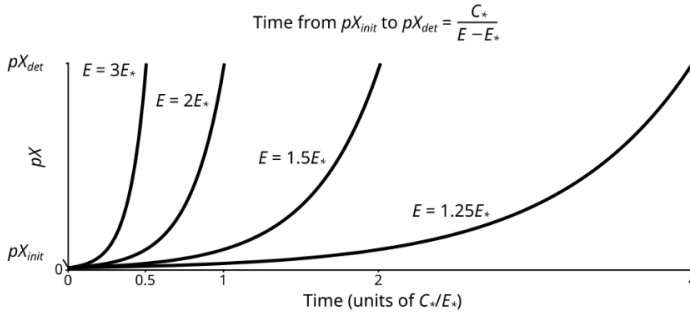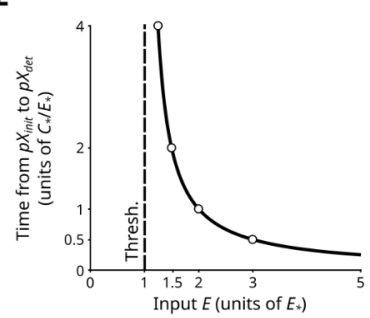
$$\frac{\mathrm{d}(pX)}{\mathrm{dt}} = k_{fb} * E * X * pX - k_{rev} * pX$$

Input thresh.

$$E_* = \frac{k_{rev}}{k_{fb} * X_{tot}}$$

Delay multi.

$$C_* = \frac{\ln(pX_{det} / pX_{init})}{k_{fb} * X_{tot}}$$

Input reciprocal time law

$$\text{Time from } pX_{init} \text{ to } pX_{det} = \frac{C_*}{E - E_*}$$

D Time from pX_{init} to $pX_{det} = \frac{C_*}{E - E_*}$

F

G
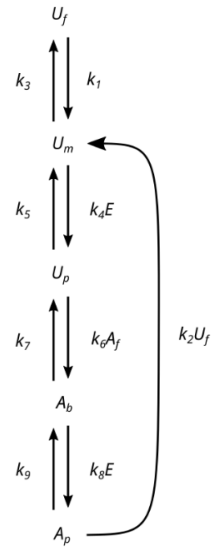
(*Figure caption continued from the previous page*) **Figure A.7: Input-coupled positive feedback produces threshold and reciprocal activation delay behavior.** **(A)** Rate equations for minimal model of input-coupled positive feedback circuit as in **Figure 1.6A**. Parameters E_* and C_* govern input threshold and reciprocal activation delay, respectively. **(B)** Rate analyses for example values of E below or above the input threshold. Forward ($k_{fb} * E * X * pX$) and reverse ($k_{rev} * pX$) reaction rates are plotted (methods). Stable steady states (SSS) and unstable steady states (USS) are identified. **(C)** Steady state analysis illustrating the system's transcritical bifurcation (TCB) that defines the input threshold (methods). For input, E, levels below the TCB, the system has one stable steady. For input, E, values above the TCB, the system has two stable states, one stable and one unstable (B, right). **(D)** Exponential growth of pX from pX_{init} to pX_{det} for various values of E (methods). Equation describing hyperbolic relationship between E and time to reach pX_{det} is shown. **(E)** Relationship between E and time to reach pX_{det} (methods). Examples from (F), marked with empty circles. **(F)** Parameterized more complete model of the PINK1/Parkin circuit. Variables are defined: Parkin, A; Ubiquitin, U; PINK1, E. Numbered rate constants "k_i" are indexed by step. **(G)** Simple schematic of the model. Rate of each step obtained by multiplying the source moiety (e.g. U_f) by the rate shown (e.g. k_1).

A

Counts (proportion) — anti-Pink1^mito intensity (AFU/px; PINK1^mito concentration)

Plate cells: HeLa (parental) +/- CCCP 3h
Express: PINK1 transfection
Fix
Plate cells: HeLa + MtTether + Parkin
+ Raplog (3-24h) 200nM

Bleach FPs, Stain, & image
anti-PINK1 (Cy5)
anti-Parkin (TRTIC)
anti-TOM20 (FITC)

Compare:
endogenous PINK1 induction
(Parental + CCCP) versus
measured PINK1 input threshold

Untreated (Parental)
CCCP 3h (Parental)
Rapalog 3h (synthetic circuit)

Measured input threshold

B CMPD39 (1uM) inhibitior of USP30

D Time of Parkin^mito recruitment (h) — Mean PINK1^mito concentration (AFU/pixel)
Vehicle — Input threshold
CMDP39 — Activation delay hyperbola

C
Vehicle ( )   CMPD39 ( )
Max Parkin^mito loc. (unitless)
73.2   68.9

$y=281/(x-73.2)$ $R^2 = 0.878$
$y=238/(x-68.9)$ $R^2 = 0.884$
Time of Parkin^mito recruitment (h)
Mean PINK1^mito concentration (AFU/pixe)

E
Input threshold (AFU/pixel)
Vehicle   CMPD39   *

Delay multiplier (h*AFU/pixel)
Vehicle   CMPD39   ***

(*Figure caption on the next page*)

74

(*Figure caption continued from the previous page*) **Figure A.8: Additional characterization of the PINK1/Parkin synthetic circuit.** **(A)** Endogenous PINK1^{mito} levels are much lower than that of the synthetic circuit. Comparison of endogenous PINK1^{mito} levels following CCCP treatment versus ectopically expressed PINK1^{mito} levels following rapalo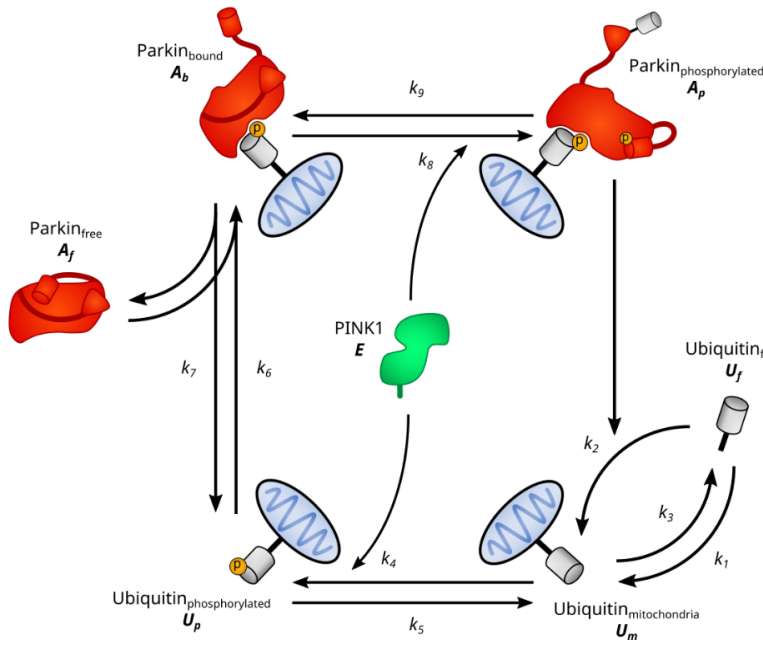g treatment for single cells (methods). The measured PINK1 input threshold is noted for reference. Schematic: experimental approach. FPs: fluorescent proteins. Imaging channels noted. Schematic bar lengths not to scale. **(B)** Chemical structure of the USP30 inhibitor, CMPD39. **(C)** Quantification of circuit behaviors from live-cell data. CMPD39 or vehicle treatment begun 2 hours prior to rapalog treatment (methods). Points: individual cells, colored by local point density. Data from four experimental replicates was pooled. **(D)** Threshold and hyperbolas from (C), overlaid. **(E)** Bootstrap statistical analysis of input threshold and delay scaler values for data in (C). Mean, 95% confidence intervals, and statistical significance calculated by bootstrap analysis (B=10,000). Bonferroni multiple comparison adjustment. *p<0.05; ***p<0.001.

APPENDIX B

Mathematical analysis of input-coupled positive feedback and emergent behaviors

B.1 General framework

B.1.1 Assumptions and conclusions

We consider two models of increasing complexity for the dynamics in the system describing PINK1–Parkin–Ubiquitin on a Mitochondrion discussed in the main body of the paper. Simplifying somewhat, we may say that in the experiment the amount $P(t)$ at time t of Parkin on a mitochondrion is tracked as it grows until it reaches a certain detection level P_{det}. The initial amount of Parkin P_{init} is assumed to be much smaller than the detection level P_{det}. This yields a measurement of the time T it takes the Parkin level to grow from P_{init} to P_{det}. The level E of PINK1 affects the rate at which Parkin increases and thus the experiment gives us a measurement of the growth time T as a function of the PINK1 level E.

The main assumptions concerning the system that we make are

i. The system contains a positive feedback mechanism

ii. PINK1 acts as a catalyst: some of the reaction rates in the system increase when the amount of PINK1 is increased

iii. P_{init} is much smaller than P_{det}

iv. The rate at which free Ubiquitin spontaneously moves to the mitochondrion is relatively small and may be ignored

v. The amounts of free Ubiquitin and Parkin are large compared to P_{det} and may be considered constant

These assumptions lead to the following consequences:

1) Exponential Growth: The amount of Parkin grows (or decays) exponentially; if $P(t)$ is the amount of Parkin at time t, then the models predict $P(t) \approx P_{\text{init}} e^{\lambda_E t}$, where the growth rate λ_E depends on the many reaction rates in the model, and in particular on the amount E of PINK1 in the system.

77

2) Threshold for circuit activation: There is a critical value E_* such that $\lambda_E < 0$ when $E < E_*$ and such that $\lambda_E > 0$ when $E > E_*$. This means that if the PINK1 amount is below E_* the Parkin levels will decrease exponentially, and if the PINK1 amount exceeds E_* then Parkin will grow exponentially.

3) Time to detection decreases with increasing PINK1 levels: The exponent λ_E is an increasing function of the PINK1 level E. When $\lambda_E > 0$ the Parkin level grows exponentially according to

$$P(t) \approx P(0)e^{\lambda_E t}.$$

Let P_{det} be the minimal level at which Parkin is detected, and assume that the initial amount P_{init} of Parkin is small compared to P_{det}. If the growth rate λ_E is negative then the amount $P(t)$ of Parkin will only decay and thus never reach the detection level. On the other hand, if the growth rate λ_E is positive, then the detection time $T_{\mathrm{det}}(E)$ follows from

(1) $\qquad P(T_{\mathrm{det}}) = P_{\mathrm{det}} \iff P_{\mathrm{init}}e^{\lambda_E T_{\mathrm{det}}} = P_{\mathrm{det}} \iff T_{\mathrm{det}} = \dfrac{\ln(P_{\mathrm{det}}/P_{\mathrm{init}})}{\lambda_E}.$

For each of the models we find that the growth rate λ_E increases when E is increased, which therefore implies that the time to detection T_{det} is a decreasing function of E.

B.1.2 The inverse law

In the minimal model one finds that there is a minimal PINK1 level E_* such that the system does not activate if $E \leq E_*$, in which case the time to detection should be considered infinite. For $E > E_*$ the time to detection in the minimal model is given by an inverse law of the form

(2) $\qquad T_{\mathrm{det}} = \dfrac{C_*}{E - E_*}$

for some constant C_*, i.e. the time to detection is inversely proportional to $E - E_*$, which is the amount of PINK1 above the critical value E_*. See (Eq. 11) for a derivation of this law in the minimal model case.

In the general model the inverse law still holds approximately. We can justify this theoretically for values of E close to the critical level E_*, and also for very large values of E. Numerical computations (**Figure B.1**) indicate that the approximation also holds for intermediate PINK1 levels.

For PINK1 values E that are close to the critical value E_* it follows from Lemma 4 that

$$\frac{\partial \lambda}{\partial E}(E_*) > 0.$$

If $E \approx E_*$ then

$$\lambda(E) \approx \frac{\partial \lambda}{\partial E}(E_*)(E - E_*),$$

and thus, if $E > E_*$ and if $E - E_*$ is small, then

$$(3) \qquad T_{\text{det}}(E) = \frac{\ln P_{\text{det}}/P_{\text{init}}}{\lambda_E} \approx \frac{C_*}{E - E_*}, \quad \text{with } C_* = \frac{\ln\left(P_{\text{det}}/P_{\text{init}}\right)}{\frac{\partial \lambda}{\partial E}(E_*)}.$$

We will also show that as $E \to \infty$, the dominant eigenvalue converges to a limiting value λ_∞ (see (Eq. 15)), and that $\lambda(E)$ is a strictly increasing function of E for all $E > E_*$. It follows that $T_{\text{det}}(E)$ has a limiting value T_∞ for very large E. Moreover, (Eq. 15) also implies that, for a suitably chosen constant C_∞ depending on the parameters k_i, one has

$$(4) \qquad T_{\text{det}}(E) \approx \frac{C_\infty}{E - E_*} + T_\infty.$$

Thus the graph of T_{det} vs. E has both horizontal and vertical asymptotes, and approaches both asymptotes like a hyperbola.

B.1.3 General form of the models

In each of the models we have a vector

$$S(t) = \begin{bmatrix} s_1(t) \\ \vdots \\ s_n(t) \end{bmatrix}$$

79

containing the total amounts of the components that the model tracks, such as Parkin, Ubiquitin, (phosphorylated or not), or combinations of these. Using mass action kinetics we arrive at a system of differential equations governing the time dependence of $S(t)$. Assuming that we only consider the system when the amounts of non-free Parkin and Ubiquitin are small, we arrive at a linear system

(5) $S'(t) = \mathcal{M}S(t),$

where

- E is the amount of PINK1 in the system; this quantity is assumed to be kept constant;
- $\mathcal{M}$ is a matrix containing the reaction rates, and which can be further decomposed as

   $\mathcal{M} = \mathcal{M}_0 + E\mathcal{M}_1.$

   The matrix $\mathcal{M}_0$ contains the rates at which reactions take place in the absence of PINK1, while $\mathcal{M}_1$ accounts for the change in the reaction rates caused by the presence of PINK1.

B.1.4 Eigenvalue analysis of the models

Using the method of eigenvalues and vectors one shows that the general solution of a linear equation such as (Eq. 5) is a superposition of exponentially growing or decaying terms, i.e.

(6) $S(t) = e^{\lambda_1 t}V_1 + e^{\lambda_2 t}V_2 + \cdots + e^{\lambda_n t}V_n$

in which $\lambda_1, \ldots, \lambda_n$ are the eigenvalues of the matrix $\mathcal{M}$, $V_1, \ldots, V_n$ are corresponding eigenvectors. Since we are interested in the time it takes $S(t)$ to grow from a small initial amount to the detection value, we want to consider the fastest growing term(s) in (Eq. 6), i.e. the terms corresponding to the largest eigenvalues λ_i. In studying the eigenvalues $\lambda_1, \ldots, \lambda_n$ we note that in all versions of our model the matrix $\mathcal{M}$ has non-negative off-diagonal entries, and is irreducible. This implies, by the Perron-Frobenius theorem, that $\mathcal{M}$ has a unique dominant eigenvalue. If we renumber the eigenvalues so that λ_{dom}, is the dominant eigenvalue, then

i. λ_{dom} is a real eigenvalue of $\mathcal{M}$ (not a complex eigenvalue)

ii. every other (possibly complex) eigenvalue μ of $\mathcal{M}$ satisfies $\operatorname{Re}\mu < \lambda_{\text{dom}}$

iii. corresponding to the eigenvalue λ_{dom}, the matrix $\mathcal{M}$ has positive left and right eigenvectors $W_{\text{dom}}, V_{\text{dom}}$ respectively; by definition these satisfy

$$\mathcal{M}V_{\text{dom}} = \lambda_{\text{dom}}V_{\text{dom}}, \qquad \mathcal{M}^\top W_{\text{dom}} = \lambda_{\text{dom}}W_{\text{dom}}.$$

They can be normalized so that $\langle W_{\text{dom}}, V_{\text{dom}} \rangle = 1$.

The dominant eigenvalue tells us the largest exponential rate with which solutions to (Eq. 5) can grow. More precisely, the eigenvalue decomposition (Eq. 6) contains one term corresponding to the dominant eigenvalue λ_{dom}. If we denote this term by $s(t)V_{\text{dom}}$ and group the remaining terms into a slower growing component $S^\circ(t)$ then we have

(7) $\qquad S(t) = s(t)V_{\text{dom}} + S^\circ(t), \qquad \langle W_{\text{dom}}, S^\circ(t) \rangle = 0.$

The left-eigenvector W_{dom} allows one to find the coefficient $s(t)$ from the vector $S(t)$ via

$$s(t) = \langle W_{\text{dom}}, S(t) \rangle.$$

By taking the inner product with W_{dom} on both sides in (Eq. 5) one finds that the V_{dom} component of S satisfies an ordinary differential equation

(8) $\qquad s'(t) = \lambda_{\text{dom}}s(t),$

whose solution can be written as

(9) $\qquad s(t) = e^{\lambda_{\text{dom}}t}s(0)$

To compute the time to detection we assume that Parkin is detected when $s(t)$ reaches a specific detection value x_{det}. Then the time to detection is

$$T_{\text{det}} = \frac{1}{\lambda_{\text{dom}}} \ln \frac{s_{\text{det}}}{s(0)}.$$

B.2 The minimal PINK1-Parkin model

In our simplest model we only keep track of the Parkin in the system, assuming it exists in one of two states: on the mitochondria or free (not on the mitochondria).

Parkin on the mitochondria can bind free Parkin and this process is aided by PINK1 as an enzymatic catalyst. Parkin on the mitochondria also spontaneously leaves the mitochondria.

Our model keeps track of the following quantities:

X_{tot} total amount of Parkin in the system; a constant

X_{p} amount of Parkin on the mitochondria (referred to as "pX" in the main text)

X amount of free Parkin, $X + X_{\text{p}} = X_{\text{tot}}$

E amount of PINK1 in the system; constant in time

Since X_{tot} and E are time independent and since X_{p} and X are constrained by $X_{\text{p}}+X = X_{\text{tot}}$, the time evolution of the system is completely determined by that of X_{p}. The following differential equation takes both recruitment and degradation into account:

$$\frac{dX_{\text{p}}}{dt} = k_{\text{fb}}E(X_{\text{tot}} - X_{\text{p}})X_{\text{p}} - k_{\text{off}}X_{\text{p}}.$$

Here k_{fb} and k_{off} are reaction constants.

We make one further simplifying assumption, namely, during the observations in the experiment, prior to X_{p} detection, the total amount X_{tot} of Parkin is much larger than the amount X_{p} on the mitochondria. Thus the amount X of free Parkin remains nearly constant, approximately equal to the total amount X_{tot} of Parkin. We may therefore replace $X_{\text{tot}} - X_{\text{p}} = X$ by X_{tot}, which leads us to the differential equation

$$(10) \qquad \frac{dX_{\text{p}}}{dt} = k_{\text{fb}}EX_{\text{tot}}X_{\text{p}} - k_{\text{off}}X_{\text{p}} = (k_{\text{fb}}EX_{\text{tot}} - k_{\text{off}})X_{\text{p}}.$$

The coefficient $k_{\text{fb}}EX_{\text{tot}} - k_{\text{off}}$ is constant in time, so this differential equation is of the type $\frac{dx}{dt} = kx$, and its solution is given by the exponential growth formula $x(t) = e^{kt}x(0)$. In terms of

X_{p} we get

$$X_{\text{p}}(t) = e^{(k_{\text{fb}}EX_{\text{tot}} - k_{\text{off}})t}X_{\text{p}}(0).$$

Indeed, equation (Eq. 10) is of the form (Eq. 5), if one lets $S(t)$ be the vector with only one component $S(t) = [X_{\text{p}}(t)]$, and if one lets $\mathcal{M}$ be the 1×1-matrix $\mathcal{M} = [k_{\text{fb}}EX_{\text{tot}} - k_{\text{off}}]$. The dominant (and only) eigenvalue of $\mathcal{M}$ is

$$\lambda_E = k_{\text{fb}}EX_{\text{tot}} - k_{\text{off}}.$$

However, since both the vector $S(t)$ and the matrix $\mathcal{M}$ only have one component, the eigenvalue analysis is not needed to solve the differential equation (Eq. 10) in this case.

In the experiment one begins with a given small amount $X_{\text{p}}(0)$ of Parkin and measures how long it takes before the amount $X_{\text{p}}(t)$ of Parkin reaches a fixed detectable level, $X_{\text{p,det}}$. By solving the equation $X_{\text{p}}(t) = X_{\text{p,det}}$ for t we find, as announced in (Eq. 2),

$$(11) \quad T_{\text{det}}(E) = \frac{\ln \frac{X_{\text{p,det}}}{X_{\text{p}}(0)}}{k_{\text{fb}}X_{\text{tot}}E - k_{\text{off}}} = \frac{\frac{1}{k_{\text{fb}}X_{\text{tot}}} \ln \frac{X_{\text{p,det}}}{X_{\text{p}}(0)}}{E - E_*} = \frac{C_*}{E - E_*}.$$

It follows from (Eq. 10) that the critical value of E, at which the systems "switches on", is

$$E_* = \frac{k_{\text{off}}}{k_{\text{fb}}X_{\text{tot}}},$$

while the constant C_* in the inverse law (Eq. 2) is given by

$$C_* = \frac{1}{k_{\text{fb}}X_{\text{tot}}} \ln \frac{X_{\text{p,det}}}{X_{\text{p}}(0)}.$$

B.3 The full model

B.3.1 The nonlinear model

Here we consider a more complete model for the PINK1-Parkin system. The full model is nonlinear, but by considering only the initial growth phase we can reduce the system to a linear

set of differential equations. We then observe the existence of a dominant growth rate λ_{dom} and analyze its dependence on the parameters in the model.
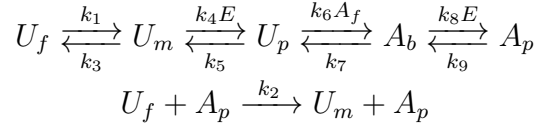
The following variables appear in the full model

U_f, U_m, U_p: Three forms of Ubiquitin: free, mitochondrial, and phosphorylated

A_f, A_b, A_p: Three forms of Parkin: free, bound, and phosphorylated

E: The amount of PINK1 present in the system; a constant.

We assume that the system is governed by the following reactions (see model schematic in Fig. S5F-G):

$$U_f \underset{k_3}{\overset{k_1}{\rightleftarrows}} U_m \underset{k_5}{\overset{k_4 E}{\rightleftarrows}} U_p \underset{k_7}{\overset{k_6 A_f}{\rightleftarrows}} A_b \underset{k_9}{\overset{k_8 E}{\rightleftarrows}} A_p$$

$$U_f + A_p \xrightarrow{k_2} U_m + A_p$$

Assuming mass-action kinetics, the variables $U_f, U_m, U_p, A_f, A_m, A_p$ evolve according to the following set of differential equations

$$\frac{dU_f}{dt} = -k_1 U_f - k_2 U_f A_p + k_3 U_m$$

$$\frac{dU_m}{dt} = k_1 U_f + k_2 U_f A_p - k_3 U_m - k_4 E U_m + k_5 U_p$$

$$\frac{dU_p}{dt} = k_4 E U_m - k_5 U_p - k_6 U_p A_f + k_7 A_b$$

$$\frac{dA_f}{dt} = -k_6 U_p A_f + k_7 A_b$$

$$\frac{dA_b}{dt} = k_6 U_p A_f - k_7 A_b - k_8 E A_b + k_9 A_p$$

$$\frac{dA_p}{dt} = k_8 E A_b - k_9 A_p$$

B.3.2 Linearization assuming abundant free Parkin and Ubiquitin

We can simplify the model by assuming that A_f and U_f are nearly constant because free Parkin and Ubiquitin are abundantly present. This leads to a reduced system with four components

U_m, U_p, A_b, A_p, which satisfy the following four linear differential equations:

$$\frac{dU_m}{dt} = -(k_3 + k_4E)U_m \qquad\qquad +k_5U_p \qquad\qquad\qquad +k_2U_fA_p$$

$$\frac{dU_p}{dt} = \qquad k_4EU_m - (k_5 + k_6A_f)U_p \qquad\qquad +k_7A_b$$

(12)

$$\frac{dA_b}{dt} = \qquad\qquad\qquad +k_6A_fU_p - (k_7 + k_8E)A_b \quad +k_9A_p$$

$$\frac{dA_p}{dt} = \qquad\qquad\qquad\qquad\qquad k_8EA_b \quad -k_9A_p$$

This linear system is of the form $X'(t) = \mathcal{M}X(t)$ (see (Eq. 5)) where

$$X(t) = \begin{bmatrix} U_m \\ U_p \\ A_b \\ A_p \end{bmatrix}$$

The matrix in this linear system is

$$\mathcal{M} = \begin{bmatrix} -k_3 - k_4E & k_5 & 0 & k_2U_f \\ k_4E & -k_5 - k_6A_f & k_7 & 0 \\ 0 & k_6A_f & -k_7 - k_8E & k_9 \\ 0 & 0 & k_8E & -k_9 \end{bmatrix}$$

Assuming all reaction rates k_i as well as the quantities E, A_f, U_f are positive, the matrix $\mathcal{M}$ satisfies the description on Eigenvalue Analysis surrounding (Eq. 6) in this appendix, i.e.

- the off-diagonal entries of $\mathcal{M}$ are non negative
- the matrix $\mathcal{M}$ is irreducible

This implies that $\mathcal{M}$ has a dominant eigenvalue λ_{dom} and corresponding left- and right-eigenvectors

$$W_{\text{dom}} = \begin{pmatrix} w_1 \\ w_2 \\ w_3 \\ w_4 \end{pmatrix}, \qquad V_{\text{dom}} = \begin{pmatrix} v_1 \\ v_2 \\ v_3 \\ v_4 \end{pmatrix},$$

for which $\mathcal{M}^\top W_{\text{dom}} = \lambda_{\text{dom}} W_{\text{dom}}, \quad \mathcal{M} V_{\text{dom}} = \lambda_{\text{dom}} V_{\text{dom}}$.

Lemma 1. *The dominant eigenvalue is a differentiable function of the parameters k_2, k_3, ..., k_9, as well as E, A_f, and U_f.*

Proof. This follows from the fact that the dominant eigenvalue is a simple eigenvalue, and that simple eigenvalues of any matrix are differentiable functions of the entries of the matrix $\mathcal{M}$. $\square$

We will show that the dominant eigenvalue turns out to be a monotone function of the parameters, at least when $\lambda_{\text{dom}} \geq 0$. The following property of the left eigenvectors W_{dom} will help in the analysis of the derivatives of λ_{dom} with respect to the parameters.

Lemma 2. *If $\lambda_{\text{dom}} \geq 0$ and if the parameters k_2, k_3, ..., k_9, as well as E, A_f, and U_f are all positive, then the entries of the left eigenvector are increasing:*

(13) $\quad w_1 < w_2 < w_3 < w_4$.

Proof. Expanding the eigenvalue equation $\mathcal{M}^\top W_{\text{dom}} = \lambda_{\text{dom}} W_{\text{dom}}$ and rearranging terms we get

$$-k_3 w_1 + k_4 E(w_2 - w_1) = \lambda_{\text{dom}} w_1$$

$$k_5(w_1 - w_2) + k_6 A_f(w_3 - w_2) = \lambda_{\text{dom}} w_2$$

$$k_7(w_2 - w_3) + k_8 E(w_4 - w_3) = \lambda_{\text{dom}} w_3$$

$$k_2 U_f w_1 + k_9(w_3 - w_4) = \lambda_{\text{dom}} w_4$$

Using the assumption that $\lambda_{\text{dom}} \geq 0$ we conclude from the first equation

$$k_4 E(w_2 - w_1) = \lambda_{\text{dom}} w_1 + k_3 w_1 \geq k_3 w_1 > 0 \implies w_2 - w_1 > 0.$$

The second equation then implies

$$k_6 A_f(w_3 - w_2) = \lambda_{\text{dom}} w_2 + k_5(w_2 - w_1) > 0 \implies w_3 - w_2 > 0.$$

Finally the third equation leads to

$$k_8 E(w_4 - w_3) = \lambda_{\text{dom}} w_3 + k_7(w_3 - w_2) > 0 \implies w_4 - w_3 > 0.$$

$\square$

Lemma 3. *Let z be one of the parameters k_2, k_3, ..., k_9, or E. If the left and right eigenvectors are normalized by $\langle W_{\text{dom}}, V_{\text{dom}} \rangle = 1$, then the derivative of λ_{dom} with respect to z is given by*

(14)
$$\frac{\partial \lambda_{\text{dom}}}{\partial z} = \left\langle W_{\text{dom}}, \frac{\partial \mathcal{M}}{\partial z} \cdot V_{\text{dom}} \right\rangle$$

Proof. Differentiate the relation $\mathcal{M} V_{\text{dom}} = \lambda_{\text{dom}} V_{\text{dom}}$ with respect to z to get

$$\mathcal{M} \frac{\partial V_{\text{dom}}}{\partial z} + \frac{\partial \mathcal{M}}{\partial z} \cdot V_{\text{dom}} = \lambda_{\text{dom}} \frac{\partial V_{\text{dom}}}{\partial z} + \frac{\partial \lambda_{\text{dom}}}{\partial z} V_{\text{dom}}$$

Take the inner product with W_{dom} on both sides:

$$\left\langle W_{\text{dom}}, \mathcal{M} \frac{\partial V_{\text{dom}}}{\partial z} \right\rangle + \left\langle W_{\text{dom}}, \frac{\partial \mathcal{M}}{\partial z} \cdot V_{\text{dom}} \right\rangle = \left\langle W_{\text{dom}}, \lambda_{\text{dom}} \frac{\partial V_{\text{dom}}}{\partial z} \right\rangle + \frac{\partial \lambda_{\text{dom}}}{\partial z} \langle W_{\text{dom}}, V_{\text{dom}} \rangle.$$

Since W_{dom} is a left eigenvector, this implies

$$\lambda_{\text{dom}} \left\langle W_{\text{dom}}, \frac{\partial V_{\text{dom}}}{\partial z} \right\rangle + \left\langle W_{\text{dom}}, \frac{\partial \mathcal{M}}{\partial z} \cdot V_{\text{dom}} \right\rangle = \lambda_{\text{dom}} \left\langle W_{\text{dom}}, \frac{\partial V_{\text{dom}}}{\partial z} \right\rangle + \frac{\partial \lambda_{\text{dom}}}{\partial z} \langle W_{\text{dom}}, V_{\text{dom}} \rangle.$$

Cancelling the first terms on both sides and then using $\langle W_{\text{dom}}, V_{\text{dom}} \rangle = 1$ leads to (Eq. 14). $\square$

Lemma 4. *As long as the dominant eigenvalue λ_{dom} is nonnegative, it is an increasing function of k_2, k_4, k_6, k_8 (forward reactions), and E, while it is a decreasing function of k_3, k_5, and k_7 (reverse reactions).*

Proof. Using the previous Lemma we can compute the derivative of λ_{dom} with respect to any of the parameters. Lemma 2 then tells us the sign of the derivative. Computing this for each of the parameters leads to the following result:

z	$\frac{\partial \lambda_{\mathrm{dom}}}{\partial z} = \langle W_{\mathrm{dom}}, \frac{\partial \mathcal{M}}{\partial z} V_{\mathrm{dom}} \rangle$		
k_2	$U_f w_1 v_4 > 0$	increasing	always
k_3	$-w_1 v_1 < 0$	decreasing	always
k_4	$E v_1 (w_2 - w_1) > 0$	increasing	if $\lambda_{\mathrm{dom}} \geq 0$
k_6	$A_f v_2 (w_3 - w_2) > 0$	increasing	if $\lambda_{\mathrm{dom}} \geq 0$
k_8	$E v_3 (w_4 - w_3) > 0$	increasing	if $\lambda_{\mathrm{dom}} \geq 0$
E	$k_4 v_1 (w_2 - w_1) + v_3 k_8 (w_4 - w_3) > 0$	increasing	if $\lambda_{\mathrm{dom}} \geq 0$
k_5	$v_2 (w_1 - w_2) < 0$	decreasing	if $\lambda_{\mathrm{dom}} \geq 0$
k_7	$v_3 (w_2 - w_3) < 0$	decreasing	if $\lambda_{\mathrm{dom}} \geq 0$

$\square$

B.3.3 The critical PINK1 value E_*

Under the assumption that the parameters k_2, k_3, ..., k_9, U_f, and A_f are positive we will argue that there is a critical value E_* such that $\lambda_{\mathrm{dom}} > 0$ for $E > E_*$ and $\lambda_{\mathrm{dom}} < 0$ for $E < E_*$. Moreover we analyze how E_* changes if one of the parameters k_2, k_3, ..., k_9, U_f, A_f is changed.

Lemma 5. *When $E = 0$, one has $\lambda_{\mathrm{dom}} < 0$, while for $E \to \infty$ the dominant eigenvalue converges to a positive limiting value $\lambda_{\mathrm{dom}}^\infty > 0$. In fact there is a constant Λ_∞ such that*

$$(15) \quad \lambda(E) = \lambda_\infty - \frac{\Lambda_\infty}{E} + \mathcal{O}\left(\frac{1}{E^2}\right) \qquad (E \to \infty)$$

Proof. We postpone the rather long proof to the next section. $\square$

Lemma 6. *There is a unique positive number E_* such that $\lambda_{E_*} = 0$. For all $E > E_*$ one has $\lambda_{\text{dom}} > 0$, while for $0 < E < E_*$ one has $\lambda_{\text{dom}} < 0$.*

Proof. We have just shown that $\lambda_{\text{dom}} < 0$ when $E = 0$, while $\lambda_{\text{dom}} > 0$ for large E. It follows from continuous dependence of the dominant eigenvalue on all parameters that there must exist intermediate values E_* at which λ_{dom} vanishes. In Lemma 4 we showed that whenever $\lambda_{\text{dom}} = 0$, λ_{dom} is increasing. This implies that there cannot be more than one E_* at which λ_{dom} vanishes. $\square$

Lemma 7. *The critical PINK1 level E_* is an increasing function of k_3, k_5, k_7, and a decreasing function of k_2, k_4, k_6, and k_8.*

Proof. By implicit differentiation applied to the equation $\lambda_{\text{dom}}(z, E_*) = 0$ we find that

$$\frac{\partial E_*}{\partial z} = -\frac{\partial \lambda_{\text{dom}}/\partial z}{\partial \lambda_{\text{dom}}/\partial E}.$$

The Lemma now follows from the table in Lemma 4. $\square$

B.4 Proofs of Lemma 5

We can write the matrix $\mathcal{M}$ as

$$\mathcal{M} = \mathcal{M}_0 + E\mathcal{M}_1$$

where

$$\mathcal{M}_0 = \begin{bmatrix} -k_3 & k_5 & 0 & k_2 U_f \\ 0 & -k_5 - k_6 A_f & k_7 & 0 \\ 0 & k_6 A_f & -k_7 & k_9 \\ 0 & 0 & 0 & -k_9 \end{bmatrix} \qquad \mathcal{M}_1 = \begin{bmatrix} -k_4 & 0 & 0 & 0 \\ k_4 & 0 & 0 & 0 \\ 0 & 0 & -k_8 & 0 \\ 0 & 0 & k_8 & 0 \end{bmatrix}$$

The dominant eigenvalue of $\mathcal{M}$ is the largest real root λ of the characteristic equation

$$
\begin{vmatrix}
-k_3 - k_4 E - \lambda & k_5 & 0 & k_2 U_f \\
k_4 E & -k_5 - k_6 A_f - \lambda & k_7 & 0 \\
0 & k_6 A_f & -k_7 - k_8 E - \lambda & k_9 \\
0 & 0 & k_8 E & -k_9 - \lambda
\end{vmatrix}
= 0.
$$

B.4.1 Proof of Lemma 5 when $E = 0$

We compute the characteristic polynomial for $E = 0$:

$$
\det(\mathcal{M} - \lambda) = \det(\mathcal{M}_0 - \lambda)
$$

$$
=
\begin{vmatrix}
-k_3 - \lambda & k_5 & 0 & k_2 U_f \\
0 & -k_5 - k_6 A_f - \lambda & k_7 & 0 \\
0 & k_6 A_f & -k_7 - \lambda & k_9 \\
0 & 0 & 0 & -k_9 - \lambda
\end{vmatrix}
$$

$$
= (\lambda + k_3)(\lambda + k_9)\big(\lambda^2 + (k_5 + k_7 + k_6 A_f)\lambda + k_5 k_7\big)
$$

It follows that when $E = 0$ the eigenvalues of the matrix $\mathcal{M}$ are

$$
\lambda_1 = -k_3, \quad \lambda_2 = -k_9,
$$

$$
\lambda_3, \lambda_4 = \frac{-k_5 - k_7 - k_6 A_f \pm \sqrt{(k_5 - k_7)^2 + 2(k_5 + k_7)k_6 A_f + (k_6 A_f)^2}}{2}
$$

All four eigenvalues are real and negative. The dominant eigenvalue λ_{dom} is the largest of these,

$$
\lambda_{\text{dom}} = \max\{\lambda_1, \lambda_2, \lambda_3, \lambda_4\} \text{ if } E = 0
$$

and it follows that for $E = 0$ one has $\lambda_{\text{dom}} < 0$.

B.4.2 Proof of Lemma 5 for large E

We write the characteristic polynomial as

(16) $\quad \det(\mathcal{M} - \lambda) = D_0(\lambda) + D_1(\lambda)E + D_2(\lambda)E^2$

where D_0, D_1, D_2 are polynomials in λ, which upon computation turn out to satisfy

$$
\begin{aligned}
D_0(\lambda) &= \det(\mathcal{M}_0 - \lambda) \\
&= (k_3 + \lambda)(k_9 + \lambda)\left(\lambda^2 + (k_5 + k_7 + k_6 A_f)\lambda + k_5 k_7\right) \\
&= \lambda^4 + \text{lower order terms,}
\end{aligned}
$$

$$
\begin{aligned}
D_1(\lambda) &= \lambda\left(k_4(\lambda + k_6 A_f + k_7)(\lambda + k_9) + (\lambda + k_3)(k_8\lambda + k_5 k_8 + (k_8 - k_7)k_7 A_f)\right) \\
&= (k_4 + k_8)\lambda^3 + \left[k_4(k_7 + k_9) + (k_3 + k_5)k_8 + (k_4 + k_8 - k_7)k_6 A_f\right]\lambda^2 \\
&\quad + (k_3 k_5 k_8 + k_3(k_8 - k_7)k_6 A_f)\lambda \\
&= (k_4 + k_8)\lambda^3 + \text{lower order terms,}
\end{aligned}
$$

and

$$
\begin{aligned}
D_2(\lambda) &= k_4 k_8(\lambda^2 + k_6 A_f \lambda - k_2 U_f k_6 A_f) \\
&= k_4 k_8 \lambda^2 + \text{lower order terms}
\end{aligned}
$$

For large values of E the four eigenvalues of $\mathcal{M}$ can be separated into those eigenvalues λ for which $\lambda \ll E$, and those for which λ is comparable to E or larger.

If $|\lambda| \sim E$ or $|\lambda| \gg E$ then the dominant terms in the characteristic polynomial (Eq. 16) are those that contain $\lambda^4, \lambda^3 E, \lambda^2 E^2$. Two eigenvalues are therefore approximated by the nonzero roots of

$$
\lambda^4 + (k_4 + k_8)\lambda^3 E + k_4 k_8 \lambda^2 E^2 = 0.
$$

This yields two very negative eigenvalues

$$\lambda_1 \approx -k_4 E, \quad \lambda_2 \approx -k_8 E.$$

If on the other hand $|\lambda| \ll E$ then $D_2(\lambda)E^2$ is the dominant term in the characteristic polynomial (Eq. 16), and thus two of the eigenvalues are close to the roots of $D_2(\lambda) = 0$, i.e. $\lambda^2 + k_6 A_f \lambda - k_2 U_f k_6 A_f = 0$, which are given by

$$\lambda_{\pm}^{\infty} = \frac{-k_6 A_f \pm \sqrt{(k_6 A_f)^2 + 4 k_2 U_f k_6 A_f}}{2}.$$

Of these, λ_{-}^{∞} is negative and $\lambda_{\text{dom}}^{\infty}$ is positive. Since $\lambda_{\text{dom}}^{\infty}$ is the only positive eigenvalue, it is the dominant eigenvalue.

The dominant eigenvalue therefore satisfies

$$(17) \quad \lambda_{\text{dom}} \approx \lambda_{\text{dom}}^{\infty} = \frac{-k_6 A_f + \sqrt{(k_6 A_f)^2 + 4 k_2 U_f k_6 A_f}}{2} > 0.$$

Thus we have shown that the dominant eigenvalue does indeed converge to the limiting value λ_∞. To complete the proof of Lemma 5 we now verify the asymptotic formula (Eq. 17). We can do this by recalling that λ is a solution of the characteristic equation

$$\det(\mathcal{M} - \lambda) = 0$$

which we can rewrite using (Eq. 16) as

$$D_0(\lambda) + D_1(\lambda)E + D_2(\lambda)E^2 = 0.$$

Divide both sides by E^2 to get

$$D_2(\lambda) + D_1(\lambda)E^{-1} + D_0(\lambda)E^{-2} = 0.$$

Instead of regarding this as an equation for λ and E, we introduce a new variable

$$\epsilon = \frac{1}{E}$$

which is related to λ by

(18) $\qquad D_2(\lambda) + D_1(\lambda)\epsilon + D_0(\lambda)\epsilon^2 = 0.$

Abbreviate the left hand side in this equation to $\varphi(\lambda, \epsilon) = D_2(\lambda) + D_1(\lambda)\epsilon + D_0(\lambda)\epsilon^2$. The limiting value λ_∞ is a solution of $D_2(\lambda_\infty) = 0$, so $\varphi(\lambda_\infty, 0) = 0$. Since λ_∞ is the largest root of the quadratic polynomial $D_2(\lambda)$ we have $D_2'(\lambda_\infty) > 0$. This implies

$$\frac{\partial\varphi}{\partial\lambda}(\lambda_\infty, 0) = D_2'(\lambda_\infty) \neq 0, \quad \text{and} \quad \frac{\partial\varphi}{\partial\epsilon}(\lambda_\infty, 0) = D_1(\lambda_\infty),$$

and we may therefore invoke the implicit function theorem to conclude that the solution $\lambda(\epsilon)$ of $\varphi(\lambda, \epsilon) = 0$ is a smooth function of ϵ. Its Taylor expansion begins with

$$\lambda = \lambda_\infty - \frac{D_1(\lambda_\infty)}{D_2'(\lambda_\infty)}\epsilon + \mathcal{O}(\epsilon^2).$$

Finally, after setting $\epsilon = \frac{1}{E}$, we obtain (Eq. 15), where the constant Λ_∞ is given by

$$\Lambda_\infty = \frac{D_1(\lambda_\infty)}{D_2'(\lambda_\infty)}.$$

B.5 Numerical computation of T_{det}

While there is no explicit formula that expresses the largest eigenvalue λ_∞ of the matrix $\mathcal{M}(E)$, and thus also the time to detection T_{det}, in terms of E and the parameters $k_1, \ldots, k_9, U_f, A_f$ both λ_∞ and T_{det} can be easily computed numerically for any specific given values of the parameters.

Using the `eigvals` routine from the Numpy.linalg package we produced log-log plots of $T_{\mathrm{det}} - T_\infty$ vs. $E - E_*$ (**Figure B.1**). In these plots the parameters $k_1, \ldots, k_9$ were chosen using

93

a random number generator so that $\log k_i$ is uniformly distributed with $-1 \leq \log k_i \leq +1$. After choosing the parameters k_i we normalized their product, so that $k_1 k_2 \cdots k_8 k_9 = 1$.

One sees from the simulations that plotting a log-log graph of $T_{\mathrm{det}} - T_\infty$ vs. $E - E_*$ consistently produces a nearly straight line with slope approximately equal to -1. This implies that the dependence of T_{det} on E follows the inverse law (Eq. 2).
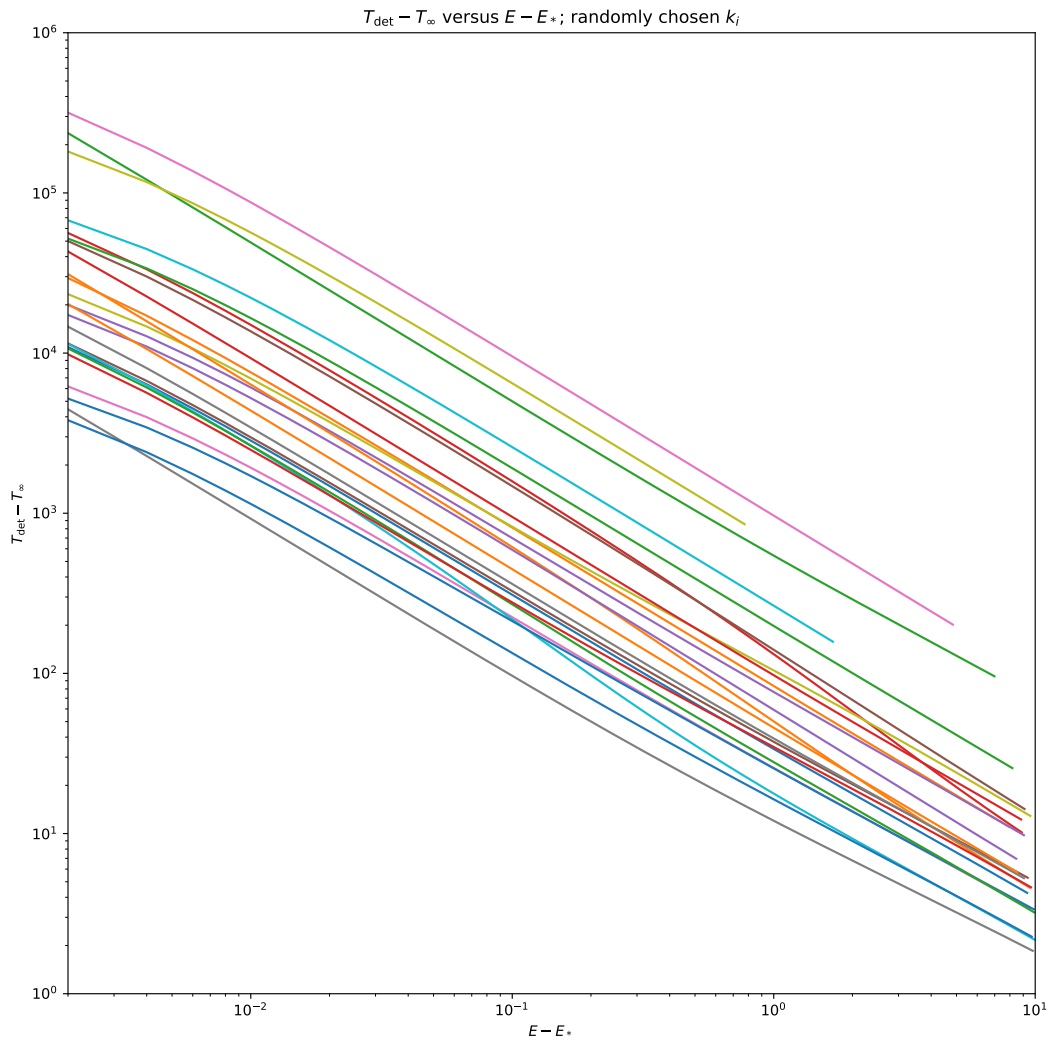
Figure B.1: Simulated behavior of the full model follows inverse time law. $T_{\mathrm{det}} - T_\infty$ vs $E - E_*$ for randomly chosen parameter values $k_1, \ldots, k_9$

Publishing Agreement

It is the policy of the University to encourage open access and broad distribution of all theses, dissertations, and manuscripts. The Graduate Division will facilitate the distribution of UCSF theses, dissertations, and manuscripts to the UCSF Library for open access and distribution. UCSF will make such theses, dissertations, and manuscripts accessible to the public and will take reasonable steps to preserve these works in perpetuity.

I hereby grant the non-exclusive, perpetual right to The Regents of the University of California to reproduce, publicly display, distribute, preserve, and publish copies of my thesis, dissertation, or manuscript in any form or media, now existing or later derived, including access online for teaching, research, and public service purposes.

DocuSigned by:

christopher waters

81182BA3B70A4E0...   Author Signature

11/27/2023

Date